Inorg. Chem. **2001,** *40,* 4389−4403

Influence of Extrinsic Factors on Electron Transfer in a Mixed-Valence Fe^{2+}/Fe^{3+} Complex: Experimental Results and Theoretical Considerations

Catalina Achim,*,† Emile L. Bominaar,‡ Richard J. Staples,† Eckard Münck,‡ and R. H. Holm*,†

Department of Chemistry and Chemical Biology, Harvard University, Cambridge, Massachusetts 02138, and Department of Chemistry, Carnegie Mellon University, 4400 Fifth Avenue, Pittsburgh, Pennsylvania 15213

Received May 11, 2001

The crystal structure of the mixed-valence complex $(NEt_4)[Fe_2(salmp)_2]\cdot x$MeCN(crystal) ($x = 2,3$) [**1**]·*x*MeCN(crystal) was determined at temperatures between 153 and 293 K. The complex shows distinct Fe^{2+} and Fe^{3+} sites over this temperature interval. Variable temperature Mössbauer spectra confirm the valence-localized character of the complex. In contrast, spectroscopic investigation of powder samples generated from [**1**]·*x*MeCN(crystal) indicate the presence of a valence-averaged component at temperatures above 150 K. To elucidate this apparent contradiction we have conducted a variable-temperature Mössbauer investigation of different forms of **1**, including [**1**]·*x*MeCN(crystal), [**1**]·2DMF(crystal), [**1**]·*y*MeCN(powder), and solution samples of **1** in acetonitrile. The low-temperature Mössbauer spectra of all forms are virtually identical and confirm the valence-localized nature of the $S = {}^9/_2$ ground state. The high-temperature spectra reveal a subtle control of electron hopping by the environment of the complexes. Thus, [**1**]·*x*MeCN(crystal) has valence-localized spectra at all explored temperatures, [**1**]·2DMF(crystal) exhibits a complete collapse into a valence-averaged spectrum over a narrow temperature range, the powder exhibits partial valence averaging over a broad temperature interval, and the solution sample shows at 210 K the presence of a valence-averaged component in a minor proportion. The spectral transformations are characterized by a coexistence of valence-localized and valence-averaged spectral components. This phenomenon cannot be explained by intramolecular electron hopping between the valence-localized states $Fe_A{}^{2+}Fe_B{}^{3+}$ and $Fe_A{}^{3+}Fe_B{}^{2+}$ in a homogeneous ensemble of complexes, but requires relaxation processes involving at least three distinguishable states of the molecular anion. Hopping rates for [**1**]·2DMF(crystal) and [**1**]·*y*MeCN(powder) have been determined from spectral simulations, based on stochastic line shape theory. Analysis of the temperature dependences of the transfer rates reveals the existence of thermally activated processes between (quasi) degenerate excited states in both forms. The preexponential factors in the rate law for the hopping processes in the [**1**]·*y*MeCN(powder) and [**1**]·2DMF(crystal) differ dramatically and suggest an important influence of the asymmetry of the complex environment (crystal) on intramolecular electron hopping. The differences between the spectra for the crystalline sample [**1**]·*x*MeCN and those for powders generated under vacuum from these crystals indicate that solvate depletion has a profound effect on the dynamic behavior. Finally, two interpretations for the three states involved in the relaxation processes in **1** are given and critically discussed (salmp = bis(salicyledeneamino)-2-methylphenolate(3-)).

1. Introduction

The valence class of binuclear mixed-valence complexes is determined by the relative strengths of vibronic trapping forces and metal−metal resonance interactions.[1−3] The former interactions prevail in valence-localized compounds (class II[4]) while the latter are predominant in valence-delocalized systems (class III). Vibronic interaction in combination with elastic forces in the complex give rise to double-well potentials with minima corresponding to the valence-localized states $M^{n+} - M^{(n+1)+}$ and $M^{(n+1)+} - M^{n+}$. Scheme 1 shows a qualitative representation of this type of potential for a symmetric (A) and asymmetric (B) dimer. The height (ΔG^*) of the barrier separating the potential minima determines the rate of thermally activated electron hopping between them. The barrier diminishes when the resonance interaction is enhanced and vanishes in the class III regime.

Scheme 1

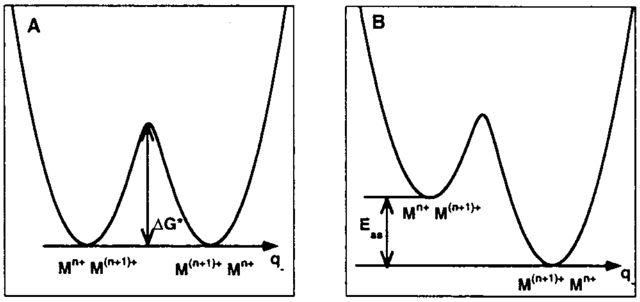

Table 1 contains examples of structurally characterized binuclear Fe(II,III) complexes with paramagnetic sites arranged

---

* To whom correspondence should be addressed.
† Harvard University.
‡ Carnegie Mellon University.

(1) Bersuker, I. B.; Borshch, S. A. *Adv. Chem. Phys.* **1992**, *81*, 703−782.
(2) Piepho, S. B.; Krausz, E. R.; Schatz, P. N. *J. Am. Chem. Soc.* **1978**, *100*, 2996−3005.
(3) Wong, K. Y.; Schatz, P. N. *Progr. Inorg. Chem.* **1981**, *28*, 369−449.
(4) Robin, M. B.; Day, P. *Adv. Inorg. Radiochem.* **1967**, *10*, 247−422.

10.1021/ic010498l CCC: $20.00

Table 1. Structurally Characterized Mixed-Valence $Fe^{2+}(S_A = 2)-Fe^{3+}(S_B = {}^5/_2)$ Complexes with N/O Coordination[a]

compound	Fe−Fe distance (Å) (temp, K)	ground spin state	loc−deloc[b]
A $[Fe_2(\mu\text{-}OH)_3(ttacn)_2](ClO_4)_2{\cdot}2CH_3OH{\cdot}2H_2O$[5]	2.51 (198)	$(9/2)_{deloc}$	
B $Fe_2(\mu\text{-}O_2CArMes_2)(\mu\text{-}OCHMe_2)_2(O_2CArMes_2)_2{\cdot}Et_2O$[6]	2.624 (173)	$(9/2)_{deloc}$	
C $[Fe_2(\mu\text{-}O_2CArTol)_4(L)_2]X$ (L,X): $(4\text{-}{}^tBuC_5H_4N,PF_6^-)$, (py, TfO^-), (THF, PF_6^-)[7]	2.663−2.713 (188)	$(9/2)_{deloc}$	
D $[Fe_2(\mu\text{-}OAc)_2L^1](ClO_4)$[8]	2.741 (295)	$(9/2)_{deloc}$	
E $Fe_2(\mu\text{-}O_2CArMes_2)(\mu\text{-}OCHMe_2)_2(O_2CArMes_2)_2$[6]	2.748 (173)	$(9/2)_{loc}$	
1 $(NEt_4)[Fe_2(salmp)_2]$[12,13]	3.10 (293)	$(9/2)_{loc}$	yes
F $[Fe_2(\mu\text{-}O)(\mu\text{-}Ph_3CCOO)_2(ttacn)_2]X$ ($X = OTf^-$, BF_4^-)[10]	3.123, 3.155 (273, 294)	$(1/2)_{loc}$	
G $[Fe_2(L^2)_2(\mu\text{-}OH)(\mu\text{-}piv)_2](ClO_4)_2$[14]	3.400 (298)	$(1/2)_{loc}$	
H $[Fe_2(bimp)(\mu\text{-}O_2CPh)_2](BPh_4)_2{\cdot}1.5CH_3CN$[9]	3.440 (295)	$(1/2)_{loc}$	yes[c]
I $[Fe_2(\mu\text{-}O)(Ph_2acac)_2(ttacn)_2](BPh_4){\cdot}C_6H_5CH_3$[11]	*d*	$(1/2)_{loc}$	*e*

[a] We have included only complexes which have identical iron coordination at the two sites of the complex, which have been structurally characterized, and for which the ground spin state has been identified. [b] Indicates that a transition from localization to delocalization on the Mössbauer time scale has been observed. [c] Detrapping on the Mössbauer time scale is strongly dependent on the anion and solvate molecules. [d] This complex contains a linear Fe−O−Fe unit. The Fe−O bond length in the two-half dimers of the asymmetric unit are 1.877 and 1.901 Å. [e] Dynamic valence detrapping. Abbreviations: ttacn, *N,N',N''*- trimethyl-1,4,7-triazacyclononane; $Mes_2ArCO_2^-$, 2,6-dimesitylbenzoate(1-); $Ar^{Tol}CO_2^-$, 2,6-di(p-tolyl)benzoate(1-); L^1, tetraiminodiphenolate(2-); bimp, 2,6(bis[bis(((1-methyl-imidazol-2-yl))methyl)amino)methyl]-4-methylphenolate(1-); piv, pivalate(1-); Ph_2acac^-, 1,3-diphenylpropane-1,3-dionate(1-).

in the order of increasing Fe−Fe distances.[5−14] The magnetic properties of these systems reveal a subtle interplay of valence delocalization and spin ordering markedly dependent on structure. Short intermetal distances give rise to strong direct metal−metal resonance interaction. According to the theory of double exchange formulated by Anderson and Hasegawa,[15] the resonance energies of the dimer spin states are given by the expression $E_\pm(S) = \pm|\beta|\ (S + {}^1/_2)/5$ in the case of a diiron complex, where S is the dimer spin and β is the electronic matrix element.[16] The largest resonance stabilization energy is attained for a state with ferromagnetically ordered iron spins, $S = {}^9/_2$. Complexes **A**−**D**, which are at the low end of the Fe−Fe distances in Table 1, are examples of mixed-valence dimers in which resonance interaction is the dominant spin coupling mechanism, resulting in ferromagnetically ordered valence-delocalized ground states, $({}^9/_2)_{deloc}$. The resonance interactions in dimers with long Fe−Fe distances are reduced below the limit where the trapping forces localize the metal valencies (class II). In this case, the double-exchange interaction gives rise to a ferromagnetic second-order contribution, $J_{DE} \sim \beta^2/U$, to the exchange-coupling constant in the HDvV Hamiltonian $-2J S_A{\cdot}S_B$, where U is an electron-correlation energy.[16] The U parameters have been estimated to be on the order of 5−15 eV for d-electrons in homovalence transition-metal complexes.[15] However, the U values for mixed-valence dimers are considerably smaller than those in homovalence systems. The parameter J also contains an antiferromagnetic contribution J_{AF} and a ferromagnetic potential exchange contribution J_F such that $J \approx J_F + J_{AF} + J_{DE}$. J_{AF} is given by a similar second-order expression as J_{DE}, namely $J_{AF} \sim -\Sigma_{ij}\,\beta_{ij}{}^2/U$ where i labels the half-filled orbitals at one metal site of the dimer and j those at the other one.[15] Since J_{DE} arises from "virtual transfer" of an electron occupying the ground orbital and J_{AF} from virtual transfer of unpaired electrons in higher-lying orbitals that have more favorable intermetal overlap characteristics for transfer than the ground orbital, J_{AF} is usually the dominant contribution to J. In complexes **F**−**I**, which are at the high end of the Fe−Fe distances in Table 1, J_{AF} is the dominant contribution to J and leads to stabilization of valence-localized $S = {}^1/_2$ ground states, $({}^1/_2)_{loc}$. In some of these complexes, the activation barrier is low enough to allow observation of thermally activated electron hopping in the Mössbauer spectra (complexes **H** and **I**).

Recently, we reported the observation of electron hopping in a $[2Fe-2S]^{1+}$ cluster of a 2-Fe ferredoxin.[17] Both hopping rate and spin ordering in the 2-Fe cluster were found to depend sensitively on the medium. This result suggested that electron transfer depends on the conformational substates of the ferredoxin. The correlation between cluster microenvironment and intramolecular electron transfer has a counterpart in synthetic mixed-valence dimers. One of the most thoroughly investigated example is the class of biferrocenium salts containing low-spin ferrous and ferric sites.[18] Detailed structural and spectroscopic investigations of these complexes led to the identification of solid-state effects on intramolecular electron-transfer rates. Several of the factors proposed as determinants for the rate of intramolecular electron hopping are phase transitions, disorder in the countercation and/or solvent, and degree of crystallinity. Hendrickson et al.[9] has given a detailed analysis of $[Fe_2(bimp)(\mu\text{-}O_2CPh)_2](BPh_4)_2$, a mixed-valence complex with high-spin iron sites and an $S = {}^1/_2$ ground state. The 295-K crystal structure of $[Fe_2(bimp)(\mu\text{-}O_2CPh)_2](BPh_4)_2{\cdot}1.5CH_3CN$ shows distinct Fe^{3+} and Fe^{2+} sites and the presence of counteranions that are asymmetrically positioned with respect to the complex cation. Surprisingly, the Mössbauer spectra recorded at the same

---

(5) Ding, X.-Q.; Bominaar, E. L.; Bill, E.; Winkler, H.; Trautwein, A. X.; Drüeke, S.; Chaudhuri, P.; Wieghardt, K. *J. Chem. Phys.* **1990**, *92*, 178−186.
(6) Hagadorn, J. R.; Que, L.; Tolman, W. B.; Prisecaru, I.; Münck, E. *J. Am. Chem. Soc.* **1999**, *121*, 9760−9761.
(7) Lee, D.; Krebs, K.; Huynh, B. H.; Hendrich, M. P.; Lippard, S. J. *J. Am. Chem. Soc.* **2000**, *122*, 5000−5001.
(8) Dutta, S. J.; Ensling, J.; Werner, R.; Flörke, U.; Haase, W.; Gütlich, P.; Nag, K. *Angew. Chem., Int. Ed. Engl.* **1997**, *36*, 152−155.
(9) Mashuta, M. S.; Webb, R. J.; McCusker, J. K.; Schmitt, E. A.; Oberhausen, K. J.; Richardson, J. F.; Buchan, R. M.; Hendrickson, D. N. *J. Am. Chem. Soc.* **1992**, *114*, 3815−3827.
(10) Payne, S. C.; Hagen, K. S. *J. Am. Chem. Soc.* **2000**, *122*, 6399−6410.
(11) Müller, M.; Bill, E.; Weyhermüller, T.; Wieghardt, K. *J. Chem. Soc., Chem. Commun.* **1997**, 705−706.
(12) Snyder, B. S.; Patterson, G. S.; Abrahamson, A. J.; Holm, R. H. *J. Am. Chem. Soc.* **1989**, *111*, 5214−5223.
(13) Surerus, K. K.; Münck, E.; Snyder, B. S.; Holm, R. H. *J. Am. Chem. Soc.* **1989**, *111*, 5501−5502.
(14) Bossek, U.; Hummel, H.; Weyhermüller, T.; Bill, E.; Wieghardt, K. *Angew Chem. Int. Ed. Engl.* **1995**, *34*, 2642−2645.
(15) Anderson, P. W. In *Magnetism*; Rado, G. T., Suhl, H., Eds.; Academic Press: New York, 1963; Vol. I, p 25−83.
(16) Blondin, G.; Girerd, J.-J. *Chem. Rev.* **1990**, *90*, 1359−1376.
(17) Achim, C.; Bominaar, E. L.; Meyer, J.; Peterson, J.; Münck, E. *J. Am. Chem. Soc.* **1999**, *121*, 3704−3714.
(18) Hendrickson, D. N. In *NATO ASI Series C*; Kluwer Academic Publishers: Dordrecht, 1991; Vol. 343, pp 67−90.

temperature revealed that the majority of the complexes appeared as valence-delocalized, of which the relative amount is a sensitive function of the solvate content of the sample.

The class II complex $[Fe_2(salmp)_2]^{1-}$ (**1**) is located at the boundary between binuclear iron species with an $(S = {}^1/_2)_{loc}$ and $(S = {}^9/_2)_{deloc}$ ground state (see Table 1). The exchange coupling is ferromagnetic in all accessible oxidation states of the complex: the diferric $[Fe_2(salmp)_2]^0$, the mixed-valence $[Fe_2(salmp)_2]^{1-}$, and the diferrous $[Fe_2(salmp)_2]^{2-}$ states.[12] The existence of ferromagnetic coupling in the homovalence complexes of this electron-transfer series indicates that J_{DE} is not the major exchange-coupling term in $[Fe_2(salmp)_2]^{1-}$. Moreover, if $J_{AF} + J_{DE}$ were a major contributor to J, the dependence of U on oxidation state would result in large differences between the exchange parameters for the pure-valence and mixed-valence complexes, in contrast to the observed relative constancy of this parameter ($J = +7$ cm^{-1} in the diferric form, $+8.6$ cm^{-1} in the mixed-valence form, and $+1.2$ cm^{-1} in the diferrous form, $H = -2JS_1\cdot S_2$). In contrast to J_{DE} and J_{AF}, which are linear in U^{1-}, J_F is determined by the first-order two-electron exchange contribution $J_F \sim \langle d_{A,i}\, d_{B,j} \,||\, d_{B,j}\, d_{A,i}\rangle$ and is independent of U.[15] Thus, among the three terms considered, potential exchange (J_F) is likely to be the principal coupling mechanism in this compound. Complex **1** is the only known example of a mixed-valence species with an $S = {}^9/_2$ ground state that exhibits a localization to delocalization transition on the Mössbauer time scale.[13] Initial variable-temperature Mössbauer spectra of $[Fe_2(salmp)_2]^{1-}$ revealed a coexistence of valence-localized and valence-averaged spectral components. The valence-average component starts to appear at ~100 K and gradually increases with temperature at the expense of the valence-localized feature to make up ~60% of the total absorption at 293 K.

To monitor structural changes in $[Fe_2(salmp)_2]^{1-}$ that accompany, and possibly influence, the spectral behavior observed in the variable-temperature Mössbauer measurements, we have determined the crystal structure of [**1**]·2DMF(crystal) at 173 K and of [**1**]·*x*MeCN(crystal) ($x = 2, 3$, see below) at temperatures between 153 and 293 K. We have used variable-temperature Mössbauer spectroscopy to investigate these two crystalline forms as well as solution samples of **1** and (solvent-depleted) powders generated from [**1**]·*x*MeCN, identified as [**1**]·*y*MeCN(powder). The results of these structural and spectroscopic investigations are presented. The coexistence of valence-localized and delocalized components observed in the Mössbauer spectra is analyzed using stochastic line shape theory. The nature of the three states required to simulate the spectra is discussed.

2. Experimental Section

Compounds are designated as follows: **1**, $(NEt_4)[Fe_2(salmp)_2]$; **2**, $[Fe_2(salmp)_2]$; **3**, $(NEt_4)_2[Fe_2(salmp)_2]$.

2.1. Preparation of Compounds. $(Et_4N)(HS)$ was procured from STREM Chemicals and recrystallized from acetonitrile/ether. The Schiff base H_3salmp (salmp = bis(salicyledeneamino)-2-methylphenolate(3-)) and [**2**]·2DMF(crystal) were prepared by published procedures.[12] Hydrated $^{57}FeCl_3$ (33% enriched) was prepared from a mixture of ^{57}Fe metal (94.7% enriched, Pennwood Chemicals) and natural abundance Fe and concentrated HCl at 80 °C followed by removal of excess HCl and partial removal of water under vacuum. The water content of the solid obtained was not determined. The following procedures were carried out using glovebox or Schlenk techniques. Compound [^{57}Fe-**2**]·2DMF(crystal) was prepared as described[12] but with use of hydrated $^{57}FeCl_3$.

$(NEt_4)[Fe_2(salmp)_2]$·*x*MeCN. The compound [^{57}Fe-**2**]·2DMF(crystal) (153 mg, 0.16 mmol) was suspended in 12 mL of acetonitrile. To this mixture was added a solution of $(Et_4N)(SH)$ (31 mg, 0.19 mmol) in 3 mL of acetonitrile. The reaction mixture was stirred for 2 h and filtered. The volume of the filtrate was reduced by one-half under vacuum. Crystals were grown directly from this solution by vapor diffusion of ether over 3d. The mother liquor was decanted, the crystals were washed with 2 × 3 mL of acetonitrile:ether 1:4 (v/v) and 2 × 3 mL of ether. Immediately after washing, crystals for X-ray diffraction and Mössbauer spectroscopy were covered with paratone oil to avoid loss of solvate. A single crystal of [**1**]·*x*MeCN(crystal) was placed in a Mössbauer sample cup made of Lucite and having an inner diameter of 2 mm. A copper collimator was used to prevent gamma radiation from reaching the detector without passing through the sample. Powder samples were obtained by grinding the crystals or by maintaining them under vacuum for several hours.

A crystalline sample after washing analyzed as [**1**]·3MeCN. Anal. Calcd for $C_{56}H_{59}N_8O_6Fe_2$: C, 63.95; H, 5.65; Fe, 10.62; N, 10.65. Found: C, 63.92; H, 5.75; Fe, 10.55; N, 10.54. Examination of bulk crystalline samples by single-crystal X-ray diffraction indicates that both di- and trisolvate crystals are formed. These crystals are isomorphous. In referring to acetonitrile solvate samples in the text, we use the designation [**1**]·*x*MeCN because of the possibility of having two or three solvate molecules per complex. When the sample was placed under vacuum for 5 h, crystallinity was lost and the resulting powder analyzed as unsolvated [**1**]. Anal. Calcd for $C_{50}H_{50}N_5O_6Fe_2$: C, 64.67; H, 5.43; Fe, 12.03; N, 7.54. Found: C, 64.37; H, 5.54; Fe, 12.11; N, 7.46. However, the ^{1}H NMR spectrum indicated that in analogous samples some acetonitrile remained, but quantitation based on NMR signal intensities is unreliable because of the paramagnetism of **1**. We term the powder samples obtained by grinding crystals or by subjecting them to vacuum [**1**]·*y*MeCN(powder) to distinguish them from the crystalline samples which we term [**1**]·*x*MeCN(crystal).

After low- and high-temperature Mössbauer spectra were collected on a single crystal, the paratone oil with which it was covered was washed off with hexane and the crystal was placed under vacuum for 5 h. The resulting powder was suspended in paratone oil and placed in the Mössbauer cup for variable-temperature Mössbauer spectroscopy.

$(NEt_4)[Fe_2(salmp)_2]$·2DMF(crystal). This compound was prepared by recrystallization of [**1**]·*x*MeCN from DMF. A crystalline product was obtained by vapor diffusion of ether into a concentrated DMF solution over 6 d.

2.2. Collection and Refinement of X-ray Data. Data were collected using a Bruker SMART CCD-based diffractometer equipped with an LT-2 low-temperature apparatus. Data were measured using ω scans of 0.3° per frame for 30 s. The structure of [**1**]·3MeCN was determined and fully refined at 153, 213, 243, and 293 K. Crystallographic data are given in Table 2. One crystal was used for obtaining the crystal structures at 153 and 213 K and another one for obtaining those at 243 and 293 K. For temperatures lower than 293 K, the crystals were coated with Apiezon T grease, glued to a glass fiber, transferred to a Siemens SMART diffractometer, and cooled in a nitrogen stream. After collection of the 243-K data set, the same crystal was covered with epoxy glue and a 293-K data set was obtained. The first 50 frames were recollected at the end of the data collection to monitor decay. None of the crystals showed decay during data collection. Cell parameters were retrieved using SMART software. Data reduction was performed using SAINT software that corrects for Lorentz polarization and decay. An empirical absorption correction (SADABS) was applied to the data. The structures were solved by direct methods using SHELXS-97 and refined by least squares on F^2 using SHELXL-97, incorporated in SHELXTL-PC v5.10. The structures were solved in the space group $P\bar{1}$(no. 2) by analysis of systematic absences. Anisotropic displacement parameters were refined for all non-H atoms except the solvate molecules. The ethyl groups of the cation are disordered over two positions and the model converged at occupations of 0.25:0.75 at 153 K, 0.31:0.69 at 213 K, 0.43:0.57 at 243 K, and 0.48:0.52 at 293 K. Hydrogen atoms on all atoms except those of solvate molecules were placed in idealized positions and refined employing a riding model with thermal parameters 1.2× those of the bonded carbon atoms. One of the acetonitrile molecules was disordered at 243 and 293 K. The following model of disorder was used in the refinement. The acetonitrile molecule was modeled with constrained C−C and C−N distances and was disordered over two positions. These positions are

Table 2. Crystallographic Data for Acetonitrile and DMF Solvates of Compound **1**

	[**1**]·3MeCN				[**1**]·2DMF
formula	$C_{56}H_{59}N_8O_6Fe_2$				$C_{56}H_{64}N_8O_8Fe_2$
fw, g mol^{-1}	1051.81				1074.84
cryst syst	triclinic				triclinic
space group	$P\bar{1}$				$P\bar{1}$
Z	2				2
T, K	153(2)	213(2)	243(2)	293(2)	173(2)
a, Å	10.873(2)	10.9045(2)	10.901(2)	10.9196(8)	12.593(5)
b, Å	12.179(2)	12.2140(2)	12.203(3)	12.2643(8)	12.969(3)
c, Å	21.544(4)	21.6780(9)	21.719(4)	21.833(1)	16.715(3)
α, deg	76.36(3)	76.298(1)	76.25(3)	76.241(1)	98.86(3)
β, deg	86.04(3)	85.948(1)	85.68(3)	85.403(1)	101.15 (3)
γ, deg	69.35(3)	69.354(1)	69.22(3)	69.212(1)	95.88(3)
V, Å^3	2593.9(9)	2624.7(1)	2623.8(9)	2655.1(3)	2621.7(9)
d_{calc}, g cm^{-3}	1.347	1.331	1.331	1.316	1.362
μ, mm^{-1}	0.618	0.611	0.611	0.604	0.615
θ range (deg)	0.97 to 27.69	0.97 to 27.53	0.97 to 28.30	0.96 to 28.29	1.26 to 28.26
GOF (F^2)	1.062	1.056	1.043	1.031	1.181
R1, wR2	0.0516,0.1433	0.0519,0.1450	0.0691,0.1901	0.0628,0.1766	0.0539,0.1405

[a] Collected using Mo Kα ($\lambda = 0.71073$ Å) radiation. [b] $R1 = \Sigma||F_0| - |F_C||/\Sigma|F_0|$. [c] $wR2 = \{\Sigma[w(F_0^2 - F_c^2)^2]/\Sigma[w(F_0^2)^2]\}^{1/2}$.

occupied alternatively in different unit cells by acetonitrile molecules in antiparallel orientations, with their CN bonds always situated in coinciding positions. One isotropic displacement parameter was refined for the carbon and nitrogen atoms in these positions.

A second 293-K data set was obtained on a different crystal. The unit cell of the latter crystal was determined at 213 K and found to agree with the unit cell determined for the other two crystals. Then the crystal was fixed in epoxy glue and the 293-K data set was obtained. That crystal contained only *two* acetonitrile molecules in each asymmetric unit, leading to the formulation [**1**]·2MeCN. We have also used SQUEEZE, a subroutine of PLATON,[19] to estimate the electron density attributable to the solvate and confirmed the presence of two solvate molecules per asymmetric unit. The crystal was isomorphous and the anion had an identical geometry as the complex anion in [**1**]·3MeCN.

The X-ray structure of [**1**]·2DMF(crystal) (previously reported at 297 K[12]) was determined at 173 K. The crystal was covered in Apiezon T grease and attached to a glass fiber. After being transferred to a Siemens diffractometer, the crystal was cooled to 173 K in a stream of cold nitrogen. Data were measured using ω scans of 0.3° per frame for 30 s. Analysis followed the same procedure as described above. The structure was solved in the $P\bar{1}$(no. 2) space group. The unit cell dimensions and content agree with the results of the previous study. There is no disorder in the countercation and cocrystallized DMF molecules. Crystallographic data are given in Table 2. (See paragraph at the end of this article for Supporting Information available.)

2.3. Mössbauer Spectroscopy. Mössbauer spectra were collected on constant-acceleration spectrometers. All isomer shifts are reported with respect to iron metal at room temperature. Data were analyzed using WMOSS software (WEB Research Co., Edina, MN).

3. Results

3.1. X-ray Analysis. Snyder et al.[12] obtained crystals of [**1**]·2DMF(crystal) by vapor diffusion of ether into a DMF solution and determined the crystal structure at 297 K. The compound crystallizes in the triclinic space group $P\bar{1}$ with two independent half-anions, one countercation, and two DMF solvate molecules per asymmetric unit. We determined the structure of this compound at 173 K (Table 2) and show that there is no phase change between 173 and 297 K. The two independent mixed-valence $[Fe_2(salmp)_2]^{1-}$ complexes have coincident $Fe_2(\mu\text{-}O)_2$ bridging units and essentially identical FeN_2O_4 coordination units. As in the original structure at 296 K, the complex has crystallographically imposed centrosymmetry, and does not exhibit distinct Fe^{2+} and Fe^{3+} sites. Because of this situation, we sought another solvate form of **1**, in which Fe^{2+} and Fe^{3+} sites are not rendered equivalent by crystallographic symmetry. This property was met by the acetonitrile solvate compounds [**1**]·xMeCN ($x = 2, 3$).

The crystal structure of [**1**]·xMeCN(crystal) was determined at four temperatures between 153 and 293 K (Table 2). These compounds also crystallize in the $P\bar{1}$ space group but, in contrast to [**1**]·2DMF(crystal), each asymmetric unit contains one complete complex anion, one countercation, and two or three solvate molecules. The structure of $[Fe_2(salmp)_2]^{1-}$ in [**1**]·3MeCN at 153 K is shown in Figure 1 together with a packing diagram that locates the three solvate molecules. There is no imposed symmetry in $[Fe_2(salmp)_2]^{1-}$. Further, there is no phase change between 153 and 293 K and no significant change in bond distances and angles. As is evident from the metric data in Table 3, distinct Fe^{2+} (Fe_A) and Fe^{3+} (Fe_B) sites are identifiable at all temperatures. All attempted fits of the 293 K data to a model in which a varying population of the two iron sites of $[Fe_2(salmp)_2]^{1-}$ is valence-delocalized failed to converge. We note the weak trend of increasing Fe(1)−O/N bond lengths with increasing temperature, in contrast with the expected reduction due to vibrational effects. This effect, however, cannot account for the 60% valence-averaged component in the Mössbauer spectra at 297 K.

Mössbauer analysis of powder samples of **1** indicates that a valence-averaged component represents 24% of the iron species at 150 K and 60% at room temperature. By using these results and the bond lengths obtained from the 153 K structure determination, we can estimate the expected metal−ligand bond lengths $\Delta_n = Fe^{n+}{-}L$ at 293 K. The inequivalent Fe sites of [**1**]·xMeCN(crystal) define a charge-ordered structure, with Fe^{2+} at A and Fe^{3+} at B. If electron hopping occurs between sites A and B in a fraction x of $[Fe_2(salmp)_2]^{1-}$ in the crystal and charge ordering prevails (no hopping) in the complementary fraction $1 - x$, the probability to find the extra electron on site B is $x/2$. Taking into account the structural changes due to hopping of the extra electron,[20] the crystallographic distances are given by

$$\bar{\Delta}_3 = {}^1/_2\, x\, \Delta_2 + (1 - {}^1/_2\, x)\Delta_3 \qquad \text{(site A)} \qquad (1a)$$

$$\bar{\Delta}_2 = (1 - {}^1/_2\, x)\Delta_2 + {}^1/_2\, x\, \Delta_3 \qquad \text{(site B)} \qquad (1b)$$

---

[19] Speck, A. L. *PLATON, A Multipurpose Crystallographic Tool*; Utrecht University: Utrecht, The Netherlands.

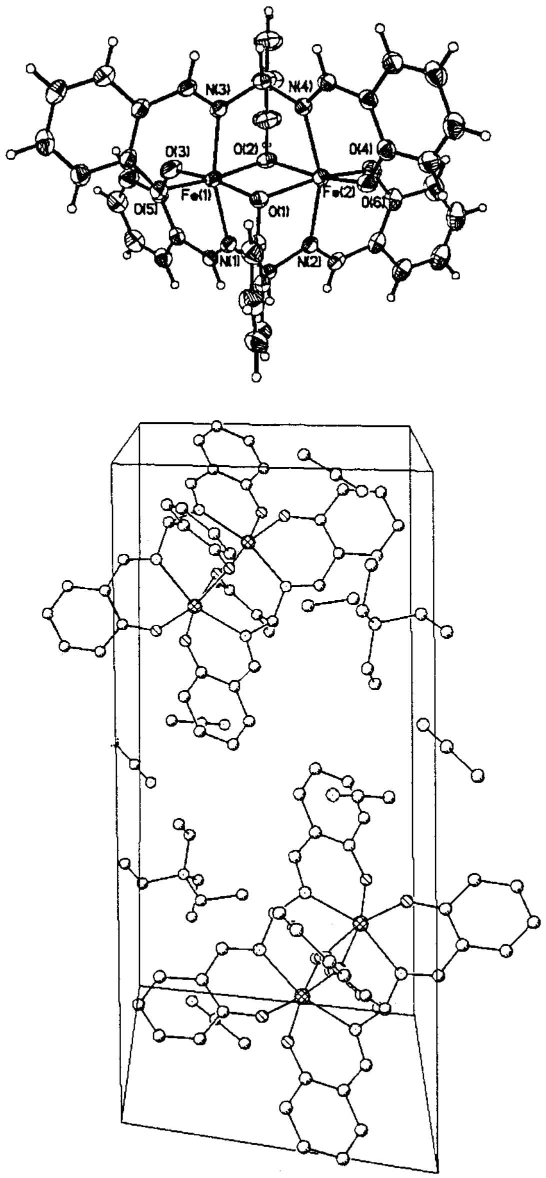

Figure 1. (A) Structure of $[Fe_2(salmp)_2]^{1-}$ in [**1**]·3MeCN at 153 K showing 50% probability ellipsoids and the atom labeling scheme. (B) Packing diagram for [**1**]·3MeCN at 153 K.

from which the true distances are obtained,

$$\Delta_3 = \bar{\Delta}_3 - \frac{x}{2(1-x)}(\bar{\Delta}_2 - \bar{\Delta}_3) \qquad (Fe^{3+}) \qquad (2a)$$

$$\Delta_2 = \bar{\Delta}_2 + \frac{x}{2(1-x)}(\bar{\Delta}_2 - \bar{\Delta}_3) \qquad (Fe^{2+}) \qquad (2b)$$

Substitution of the 153 K data for the Fe−O$_{bridge}$ ($x = 0.24$, $\bar{\Delta} = 2.186$ Å and $\bar{\Delta} = 2.007$ Å) in eqs 2 yields $\Delta_2 = 2.198$ Å and $\Delta_3 = 1.995$ Å. The latter Δ_2 and Δ_3 distances and the fraction of valence-averaged dimers x(293 K) = 0.60 can be inserted in eq 1 for estimating the averaged distances at 297 K. These values are $\bar{\Delta}_2 = 2.137$ Å and $\bar{\Delta}_3 = 2.056$ Å, from which we predict a difference ≤ 0.081 Å in the crystallographic distances for the two sites. This number is much smaller than the difference of 0.166 Å obtained by subtracting the crystallographic metal−ligand separations observed at 293 K. Thus, the structural changes are incompatible with electron hopping.[21] This surprising result prompted us to reinvestigate the Mössbauer properties of **1** and to search for alternative interpretations of the valence-averaged component.

Table 3. Selected Interatomic Distances [Å] and Angles [deg] for $[Fe_2salmp_2]^-$ in [**1**]·3MeCN

distance/angle	153 K	213 K	243 K	293 K
Fe(1)−O(1)	2.012(2)	2.014(2)	2.020(2)	2.024(2)
Fe(1)−O(2)	2.002(2)	2.006(2)	2.011(2)	2.012(3)
Fe(1)−O(3)	1.945(2)	1.948(2)	1.947(3)	1.950(3)
Fe(1)−O(5)	1.949(2)	1.950(2)	1.950(3)	1.947(3)
Fe(1)−N(1)	2.138(2)	2.138(2)	2.136(3)	2.142(3)
Fe(1)−N(3)	2.144(2)	2.146(2)	2.141(3)	2.147(3)
Fe(2)−O(1)	2.169(2)	2.170(2)	2.161(2)	2.159(3)
Fe(2)−O(2)	2.202(2)	2.202(2)	2.191(2)	2.193(3)
Fe(2)−O(4)	2.010(2)	2.008(2)	2.001(3)	2.003(3)
Fe(2)−O(6)	2.026(2)	2.028(2)	2.023(3)	2.023(3)
Fe(2)−N(2)	2.195(2)	2.199(2)	2.195(3)	2.203(3)
Fe(2)−N(4)	2.174(2)	2.176(2)	2.174(3)	2.179(3)
O(3)−Fe(1)−O(2)	92.8(1)	92.7(1)	92.9(1)	92.7(1)
O(5)−Fe(1)−O(2)	172.45(8)	172.19(8)	172.2(1)	172.0(1)
O(3)−Fe(1)−O(1)	172.06(8)	172.14(9)	172.1(1)	172.2(1)
O(5)−Fe(1)−O(1)	89.42(9)	89.81(9)	90.4(1)	90.5(1)
O(2)−Fe(1)−O(1)	89.66(8)	89.32(8)	88.62(9)	88.6(1)
O(2)−Fe(1)−N(1)	83.46(8)	83.46(8)	83.7(1)	84.1(1)
O(1)−Fe(1)−N(1)	84.06(9)	83.99(8)	83.98(9)	84.1(1)
O(2)−Fe(1)−N(3)	84.16(9)	83.99(9)	83.93(1)	83.8(1)
O(1)−Fe(1)−N(3)	86.70(9)	86.48(8)	85.92(9)	85.8(1)
O(4)−Fe(2)−O(1)	167.52(8)	167.30(8)	167.4(1)	167.2(1)
O(6)−Fe(2)−O(1)	93.46(9)	93.58(9)	94.2(1)	94.2(1)
O(1)−Fe(2)−N(4)	83.80(8)	83.62(8)	83.52(9)	83.51(9)
O(1)−Fe(2)−N(2)	81.17(8)	81.18(8)	81.18(9)	81.28(9)
O(4)−Fe(2)−O(2)	95.75(9)	95.82(9)	95.5(1)	95.3(1)
O(6)−Fe(2)−O(2)	167.48(8)	167.21(8)	167.49(9)	167.3(1)
O(1)−Fe(2)−O(2)	80.69(8)	80.50(8)	80.61(9)	80.78(9)
N(4)−Fe(2)−O(2)	81.60(8)	81.45(8)	81.57(9)	81.3(1)
N(2)−Fe(2)−O(2)	80.82(8)	80.77(8)	80.62(9)	80.5(1)
Fe(1)−O(1)−Fe(2)	95.15(8)	95.45(8)	95.71(9)	95.6(1)
Fe(1)−O(2)−Fe(2)	94.44(8)	94.68(8)	95.01(9)	94.9(1)

3.2. Mössbauer Results. We have recorded Mössbauer spectra between 4.2 and 303 K for various physical states of **1**, which are specified in Table 4. While the 4.2 K spectra of all samples were essentially the same (see below), spectra recorded above 100 K differed substantially for frozen solutions and different crystalline states of **1**. In this section we describe the spectra obtained for the various physical states.

Figure 2A shows a 4.2 K Mössbauer spectrum of an ^{57}Fe-enriched sample in a frozen acetonitrile solution of **1**. The spectrum consists of two spectral components in a 1:1 ratio, with parameters characteristic of a high-spin ferrous and a high-spin ferric site. The solid lines drawn above Figure 2A show the ferrous and ferric components separately and the line through the data shows the spectral simulation obtained by summing these components.[13] Figures 2B, 2C, and 2D show 4.2-K spectra of polycrystalline samples of [**1**]·*x*MeCN(crystal), [**1**]·*y*MeCN(powder), and [**1**]·2DMF(crystal), respectively. Except for small differences in the line widths (attributable to slightly different paramagnetic relaxation rates) and line intensities (the collection of crystals is only approximately a sample containing randomly oriented molecules), the spectra are virtually the same: all reflect a fully localized mixed-valence state. These 4.2-K spectra are very sensitive to some of the hyperfine parameters. For instance, a change of $A_y/g_n\beta_n$ from −5.7 T to −5.8 T of the ferrous site or from −11.7 T to −11.8 T of the ferric site would be readily discerned. This result indicates that at 4.2 K the electronic

---

(20) Shilov, G. V.; Ponomarev, V. I.; Atovmyan, L. O.; Gol'danskii, V. I. *J. Struct. Chem.* **1990**, *30*, 773−777.

(21) A similar incompatibility is found between the Mössbauer and crystallographic data for $[Fe_2(bimp)(\mu\text{-}O_2CPh)_2](BPh_4)\cdot xCH_3CN$.[9]

Table 4. Description of Samples Analyzed by Mössbauer Spectroscopy

sample #	sample state	comment	spectra shown
sample 1	**1** in MeCN	frozen solution	Figs. 2A, 3A
sample 2	[**1**]·2DMF(crystal)	polycrystalline	Figs. 2D, 4, 5A
sample 3	[**1**]·*x*MeCN(crystal)	selected crystals	Figs. 2B, 3B
sample 4	[**1**]·*y*MeCN(powder)	powder obtained by grinding [**1**]·*x*MeCN(crystal) with a mortar and pestle	Figs. 2C, 5B, 6
sample 5	[**1**]· *y*MeCN(powder)	powder obtained by pumping on [**1**]·*x*MeCN(crystal)	Figure 3C

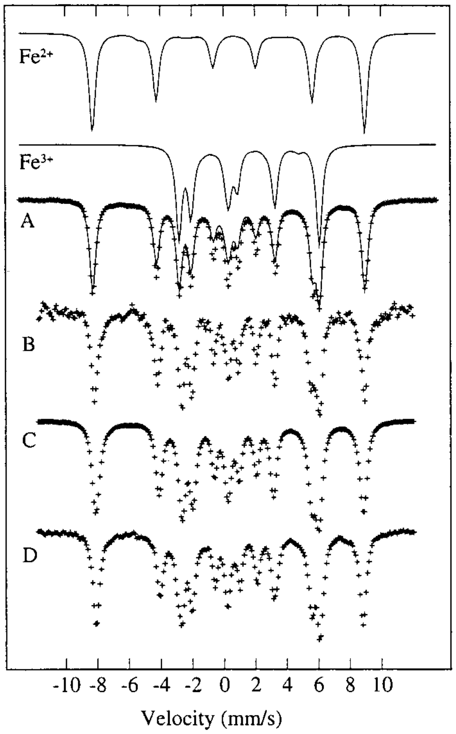

Figure 2. Mössbauer spectra of **1** recorded at 4.2 K in parallel-applied fields of 50 mT. (A) Spectrum of a frozen acetonitrile solution of **1** (sample 1); (B) Spectrum of as-isolated crystals of [**1**]·*x*MeCN (sample 3); (C) Powder sample obtained by grinding [**1**]·*x*MeCN(crystal) (sample 4); (D) As-isolated crystals of [**1**]·2DMF(crystal) (sample 2). Solid line drawn through the data of (A) is a spectral simulation for an $S = ^9/_2$ system using the parameters of Surerus et al.[13] The contributions of the Fe^{3+} and Fe^{2+} sites are outlined separately.

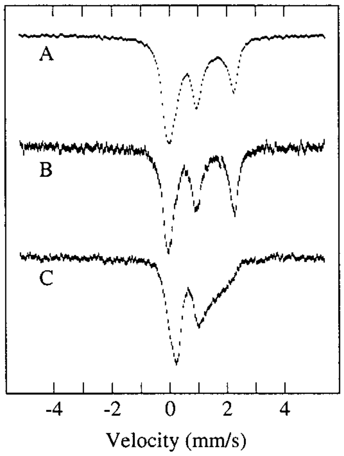

Figure 3. (A) 210-K Mössbauer spectrum of ^{57}Fe-enriched **1** dissolved in acetonitrile (sample 1); (B) 225-K Mössbauer spectrum of as-isolated crystals of [**1**]·*x*MeCN(crystal) (sample 3); (C) 240-K Mössbauer spectrum of powder sample obtained by pumping on [**1**]·*x*MeCN(crystal) (sample 5).

structure of the complex is virtually unaffected by changes in the surrounding medium.

The spectra of **1** between 10 K and about 80 K show intermediate paramagnetic relaxation and are therefore difficult to analyze. At 100 K, however, the paramagnetic relaxation is fast and gives rise to quadrupolar spectra in all samples. Figure 3 shows representative high-temperature spectra. The spectrum of Figure 3A was obtained at 210 K for **1** dissolved in acetonitrile (sample 1). This solvent melts at 227 K allowing us to record Mössbauer spectra up to 210 K, a temperature above which the recoilless fraction sharply decreases. The data of Figure 3A can be decomposed into three doublets. Two of these doublets can be assigned to a valence-localized species. One (ca. 40% of total Fe) has $\Delta E_Q = 2.31$ mm/s and $\delta = 1.06$ mm/s; these parameters are typical for a high-spin ferrous site. A second doublet, also representing ca. 40% of the iron, with $\Delta E_Q = 0.88$ mm/s and $\delta = 0.53$ mm/s belongs to the associated high-spin ferric site. A third spectral component contributes some absorption between the high-velocity lines of the ferric and ferrous sites. As discussed below, this feature reflects incipient fast-electron hopping between the ferric and ferrous sites for a small fraction of molecules in the sample.

The 225 K spectrum of Figure 3B was recorded for a collection of crystals that were deemed suitable for a crystallographic study and which were placed immediately after collection from the mother liquor under oil, [**1**]·*x*MeCN(crystal) (sample 3). The spectrum consists of two doublets with $\Delta E_Q = 2.36$ mm/s, $\delta = 1.07$ mm/s and $\Delta E_Q = 0.88$ mm/s, $\delta = 0.49$ mm/s (0.30 mm/s fwhm Lorentzian width) belonging to the ferrous and ferric sites of a complex with localized valencies. We have observed this pattern of doublets from 100 to 240 K. Except for the second-order-Doppler shift and a small decrease of the quadrupole splitting of the ferrous site (from 2.45 mm/s at 100 K to 2.36 mm/s at 240 K), the spectral pattern indicative of localization remains the same over the entire range of temperature. In particular, the spectra do not exhibit features associated with a transition to a delocalized mixed-valence state.

Figure 4 shows a series of high-temperature spectra obtained for a polycrystalline sample of [**1**]·2DMF(crystal) (sample 2). The 100 K spectrum consists of two doublets (brackets) representing an Fe^{3+} ($\Delta E_Q = 0.87$ mm/s; $\delta = 0.63$ mm/s) and an Fe^{2+} ($\Delta E_Q = 2.28$ mm/s; $\delta = 1.09$ mm/s) site. Alternative pairing of the four lines would yield the unreasonable result that the ferrous site has a larger isomer shift at 100 K than at 4.2 K. As the temperature is increased above 100 K, the absorption lines of both the ferric and the ferrous site broaden (Table 5 gives the results from simple Lorentzian fits; a refined analysis is presented below.). This broadening is accompanied by a decrease of the intensity of both doublets and the appearance of one new doublet (dashed vertical lines). The new doublet (bracket in Figure 4D) has $\Delta E_Q = 1.04$ mm/s and $\delta = 0.78$ mm/s at 185 K. For a direct comparison the 100 and 138 K spectra are plotted together in Figure 5A.

Figure 6 shows high-temperature spectra of a powder sample [**1**]·*x*MeCN(powder) (sample 4) generated by grinding crystals of [**1**]·*x*MeCN(crystal). These spectra have features not observed in samples 1, 2, and 3. Thus, the transition observed for sample 4 extends from 100 K to well above 300 K, in contrast to crystalline [**1**]·2DMF(crystal) (sample 2) which undergoes a localization to delocalization transition over a narrow temper-

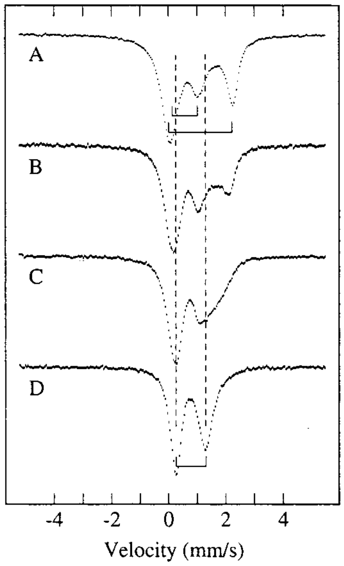

Figure 4. High-temperature Mössbauer spectra of [**1**]·2DMF (sample 2): (A) 100 K; (B) 125 K; (C) 138 K; (D) 185 K. Features of the ferric and ferrous sites are marked by brackets.

Table 5. Mössbauer Parameters Obtained from Lorentzian Fits of High-Temperature Mössbauer Spectra of [**1**]·2DMF(crystal)

temp (K)	iron site	δ (mm/s)	ΔE_Q (mm/s)	Γ^a (mm/s)
100	Fe^{2+}	1.09	2.28	0.50
	Fe^{3+}	0.64	0.85	0.60
125	Fe^{2+}	1.08	1.81	0.69
	Fe^{3+}	0.61	0.95	0.63
138	Fe^{2+}	0.96	1.56	0.71
	Fe^{3+}	0.68	0.87	0.54
150	$Fe^{2.5+}$	0.79	1.06	0.50, 0.70
200	$Fe^{2.5+}$	0.77	1.03	0.42, 0.57

[a] Line width parameter (fwhm).

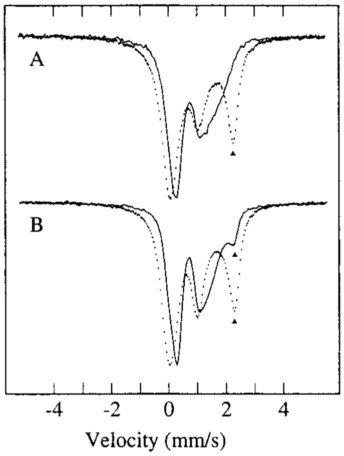

Figure 5. (A) Comparison of 100 and 138 K spectra obtained for [**1**]·2DMF (sample 2); (B) Comparison of 125 and 293 K spectra for a powder sample obtained by grinding [**1**]·*x*MeCN(crystal) (sample 4). The 293 K spectrum has been shifted by 0.08 mm/s to higher velocities to adjust for the second-order Doppler shift. Arrows mark the high-energy lines of the ferrous site.

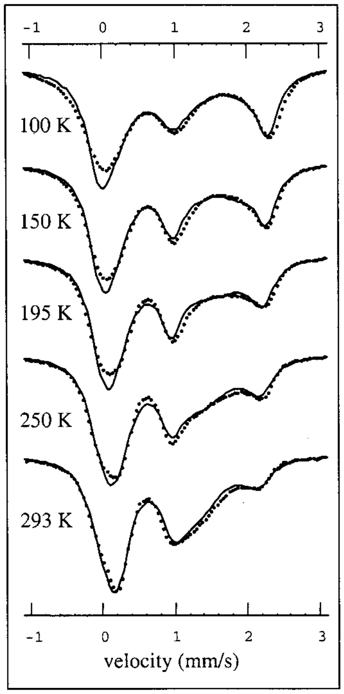

Figure 6. Variable-temperature Mössbauer spectra of polycrystalline sample of [**1**]·*y*MeCN(powder) and relaxational simulations (solid curves), based on the three-state model. Electronic parameters and rate constants used in simulations are listed in Tables 6 and 7, respectively. Vertical scales have been adjusted for presentational purposes.

ature range (roughly 100−180 K). Figure 5 shows the spectral pattern for samples 2 and 4 in the transition range. For sample 2, the transition to the delocalized state involves broadening of the spectra of the localized sites accompanied by a shift of the lines of these spectra toward the line positions characteristic of a delocalized state. For instance, the high-energy line (at 2.2 mm/s; arrow) of the ferrous site of the [**1**]·2DMF(crystal) sample broadens and moves inward as the temperature is raised. For sample 4, the position of the corresponding line (arrow) remains essentially unchanged and uniformly declines in intensity as the temperature is raised to 293 K. This observation suggests that the complex anion **1** in sample 4 has a ground state that remains localized over the entire temperature range and is gradually depopulated as the temperature is increased above 100 K. The excited states that are populated do not exhibit a pattern typical of localized states. Rather, a relaxation pattern reminiscent of the pattern in Figure 4B-D develops, suggesting that the system is activated to an excited state in which it can undergo transitions between $Fe^{2+}{}_AFe^{3+}{}_B$ and $Fe^{3+}{}_AFe^{2+}{}_B$ configurations at rates comparable with the inverse time scale of Mössbauer spectroscopy.[22] At sufficiently high temperatures, transitions between these excited-state configurations are fast and produce a single asymmetric quadrupole doublet with Mössbauer parameters identical to the average doublet observed at 185 K for [**1**]·2DMF(crystal). As a result, the spectra of Figure 6 show the coexistence of patterns characteristic of localized and delocalized species.

In the present study, samples prepared by grinding the crystals [**1**]·*x*MeCN(crystal) in a mortar exhibited complicated patterns, as shown in Figure 6. In contrast, a collection of crystals

---

(22) Throughout this paper we compare transitions between various electronic states with the "time scale of Mössbauer spectroscopy". For the processes described here this time scale is determined by the differences in quadrupole interactions and isomer shifts of the states connected by the transitions. As a guide for the reader, processes with rates slower than about 1 MHz are slow on the Mössbauer time scale. In this limit, well-defined quadrupole doublets characteristic of Fe^{3+} and Fe^{2+} sites are observed. For rates faster than ~ 20 MHz, the contributions of the states involved are averaged and one doublet with average ΔE_Q and δ-values is observed (provided $Fe^{2+}{}_AFe^{3+}{}_B$ and $Fe^{3+}{}_AFe^{2+}{}_B$ would yield the same spectra in the limit of slow fluctuation). As the transition rates increase from the slow to the fast limit, the two doublets broaden and the spectra merge towards the averaged pattern. This intermediate transition regime, where "merging" occurs, is characterized by broadened absorption patterns.

maintained under oil before collection of the Mössbauer spectra showed valence localization up to 240 K. Elemental analysis indicated that the prism-shaped crystals contained three acetonitrile solvate molecules per dimer of **1**, whereas according to the x-ray analysis two or three solvate molecules per dimer may be present, depending on the choice of the crystal. This result suggested easy loss of acetonitrile from the crystals and made us wonder whether the differences seen in the high-temperature Mössbauer spectra for [**1**]·*x*MeCN(powder) and [**1**]·*x*MeCN(crystal) reflected a different solvent content. We tested the hypothesis that solvate can be removed from a collection of crystals (such as those of sample 3) by applying a vacuum to [**1**]·*x*MeCN(crystal). Pumping on the samples shattered the crystals and yielded a fine powder, which was found to have lost solvate molecules. The question of how much acetonitrile solvate is present in the sample after the vacuum treatment is difficult to answer. With the caveat that elemental analysis must distinguish between very close percentages for [**1**]·*x*MeCN(crystal) in the cases $x = 0-3$, the analysis suggested that $x \approx 0$ after a sample had been subjected to vacuum for 5 h. On the other hand, NMR measurements indicated that some acetonitrile molecules were still present after subjecting the samples to vacuum for 5 h, but a precise quantitation of the amount based on NMR was hampered by the paramagnetism of **1**. Therefore, we cannot give an accurate value for *y* in [**1**]·*y*MeCN(powder) in samples 4 and 5, but most likely $y \approx 0,1$. Such powder samples produced Mössbauer spectra exhibiting a pattern indicating a complex transition from a localized to a delocalized mixed-valence state at temperatures above 100 K. These spectra were different for different preparations, an observation we attribute to their variable solvate content. A 240-K spectrum obtained for a powder generated by pumping 5 h on [**1**]·*x*MeCN(crystals) is shown in Figure 3C. This spectrum resembles the spectrum of [**1**]·2DMF(crystal) at 138 K (Figure 4c).

4. Discussion

4.1. Qualitative Comparison of [1]·*x*MeCN(crystal) and [1]·2DMF(crystal). The Mössbauer spectra of [**1**]·*x*MeCN(crystal) and [**1**]·2DMF(crystal) described in Section 3.2 revealed, respectively, the absence and presence of thermally activated electron transfer. The crystallographic data for these crystals indicate that the difference in electron mobility observed for the two forms is related to crystal symmetry. Thus, in [**1**]·2DMF(crystal) the iron sites of the anion are situated in identical environments, while in [**1**]·*x*MeCN(crystal) the sites experience asymmetric surroundings. We may associate these types of environment with the minima of symmetric (asymmetry parameter $E_{\mathrm{as}} = 0$) and asymmetric ($E_{\mathrm{as}} \neq 0$) potential surfaces, respectively (Scheme 1). As a result of the difference between the asymmetry parameters for the two species, the iron sites appear either as valence-averaged (DMF) or as trapped (MeCN) in the high-temperature Mössbauer spectra. An alternative interpretation, based on the dependence of the hopping rate (p') on barrier height (ΔG^*), requires substantially different ΔG^* values for the two crystalline forms, as suggested by the following considerations: The onset of delocalization in [**1**]·2DMF(crystal) at 125 K and the absence of any such effect in [**1**]·*x*MeCN(crystal) at nearly twice this temperature imply that p'_{DMF}(at 125 K) > p'_{MeCN} (at 240 K). By using the commonly employed rate law for activated electron transfer, $p'_{\mathrm{X}} = A \exp[-\Delta G^*(\mathrm{X})/k_{\mathrm{B}}T]$, it follows that $\Delta G^*(\mathrm{MeCN}) > 2\ \Delta G^*(\mathrm{DMF})$. The barrier height is the sum of inner-sphere and outer-sphere contributions, $\Delta G^* = \Delta G^*_{\mathrm{inner}} + \Delta G^*_{\mathrm{outer}}$. The large distortions in the valence-trapped structure of the complex suggest a value of a few thousand wavenumbers for $\Delta G^*_{\mathrm{inner}}$, which is on the order of energies typical for outer-sphere reorganization. With the reasonable assumption that the inner sphere contributions to the activation barrier are the same for [**1**]·2DMF(crystal) and [**1**]·*x*MeCN(crystal), i.e., $\Delta G^*_{\mathrm{inner}}(\mathrm{DMF}) \approx \Delta G^*_{\mathrm{inner}}(\mathrm{MeCN})$, it follows from the above inequality for the total barriers that $3\ \Delta G^*_{\mathrm{outer}}(\mathrm{DMF}) < \Delta G^*_{\mathrm{outer}}(\mathrm{MeCN})$. The very large increase required for $\Delta G^*_{\mathrm{outer}}$ in the case of a barrier-controlled rate makes us favor an asymmetry-controlled rate as an explanation for the differences between the electron mobility for [**1**]·*x*MeCN(crystal) and [**1**]·2DMF(crystal).

4.2. Analysis of the Mössbauer Spectra of [1]·*y*MeCN(powder) and [1]·2DMF(crystal). Electron hopping in [**1**]·*y*MeCN(powder) and [**1**]·2DMF(crystal) has a dramatic effect on the Mössbauer spectra, as can be seen in Figures 4 and 6. The spectra undergo complex transformations when the hopping rate approaches the precession frequency of the ^{57}Fe nuclei. Theories for describing time-dependent effects on spectra have been developed by several authors.[23,24] These efforts resulted in the stochastic line shape theory for simulating relaxational NMR, EPR, and Mössbauer spectra. For intramolecular electron hopping between the two sites of the diiron complex (two-state model), this theory predicts spectral merging of the quadrupole doublets for Fe^{2+} and Fe^{3+}. Our data on [**1**]·2DMF(crystal) (see below) and [**1**]·*y*MeCN(powder) show the coexistence of valence-localized and valence-averaged components. Such observations cannot be explained with any two-state model applied to a homogeneous system. While one cannot readily rule out an inhomogeneous environment in [**1**]·*y*MeCN(powder) inhomogeneities are unlikely to be present in [**1**]·2DMF(crystal) which exhibits similar spectral behavior. These observations prompted us to consider a three-state model.

A qualitative consideration of the [**1**]·*y*MeCN(powder) spectra suggests the following physical situation. The system is in a trapped valence state $\mathrm{Fe_A}^{2+}\mathrm{Fe_B}^{3+}(1)$ (denoted state 1) below 100 K. Assuming that a remnant asymmetry ($E_{\mathrm{as}} \neq 0$) persists after partial solvent depletion, the site at which the electron is trapped is unique (denoted $\mathrm{Fe_A}$), like the trapping sites in the charge-ordered structure of the crystalline precursor. By raising the temperature, a second system state $\mathrm{Fe_A}^{2+}\mathrm{Fe_B}^{3+}(2)$ (denoted state 2) is gradually thermally occupied, whereupon a dynamical variable, other than the position coordinate of the "extra" electron, is altered such that the hopping process from state 2 to a state 3, $\mathrm{Fe_A}^{3+}\mathrm{Fe_B}^{2+}(3)$, is facilitated. Thus, the metal valencies appear as $\mathrm{Fe_A}^{2+}(1)$, $\mathrm{Fe_A}^{2+}(2)$, $\mathrm{Fe_A}^{3+}(3)$ at site A and $\mathrm{Fe_B}^{3+}(1)$, $\mathrm{Fe_B}^{3+}(2)$, $\mathrm{Fe_B}^{2+}(3)$ at site B, where the state of the system is given in parentheses. In this context, the "system" includes the complex and the surroundings relevant for the hopping process. Accordingly, the term "state" specifies the electronic wave function and conformation of the complex, the positions of the solvate molecules and counterions, and possibly the states of the neighboring complexes. Transitions between the states may modify a subset of more than one of these variables. The populations of the states (denoted W_{i}, i = 1, 2, 3; $W_1 + W_2 + W_3 = 1$) depend on the relative energies and multiplicities (e.g., spin multiplicities) of the states. State 1 has the lowest energy and the higher-lying hopping states (2 and 3) are assumed to be degenerate. The rate constants $p_{\mathrm{i}\rightarrow\mathrm{j}}$ for the transfer processes between the states i and j are determined by activation barriers (see Scheme 1) and matrix elements between the localized electronic states (Section 4.3). The system is in

---

(23) Kubo, R. *J. Phys. Soc. Jpn.* **1954**, *9*, 935. Anderson, P. W. *J. Phys. Soc. Jpn.* **1954**, *9*, 316−339.

(24) Blume, M. *Phys. Rev.* **1968**, *174*, 351−358.

thermodynamic equilibrium and therefore fulfills the condition of detailed balance,

$$W_i\, p_i = W_j\, p_j \tag{3}$$

We adopt the definitions $p_u = p_{1\rightarrow 2}$ and $p_d = p_{2\rightarrow 1}$ (u and d stand for "up" and "down") and $p' = p_{2\rightarrow 3} = p_{3\rightarrow 2.}$ The latter identity follows from the assumed degeneracy of states 2 and 3 ($W_2 = W_3$) and the condition for detailed balance.

The electronic states are coupled to the ^{57}Fe nuclei of the mixed-valence dimer by magnetic and electric hyperfine interactions. Since the internal magnetic fields nearly vanish due to fast paramagnetic relaxation in the temperature range where the valence-averaged component emerges (see above), we consider only the electric hyperfine interactions. These interactions depend, in general, on which iron site and electronic state is considered,

$$H_\alpha = \delta_\alpha + \frac{1}{6}\Delta E_{Q,\alpha}(1 + \eta_\alpha{}^2/3)^{-1/2}\Big[3I_{z_\alpha}{}^2 - \frac{15}{4} + \eta_\alpha(I_{x_\alpha}{}^2 - I_{y_\alpha}{}^2)\Big] \tag{4}$$

Accordingly, the parameters are labeled by suffix α = {**N**, i}, where **N** = A, B identifies the iron site and i = 1, 2, 3 indicates the electronic state. The quadrupole interactions are expressed in the principal axes frames (x_α,y_α,z_α) of the electric field gradient (EFG) tensors ($\Delta E_{Q,\alpha}$ and asymmetry parameter η_α). Euler rotations over angles α, β, and γ specify the orientation of the EFG-tensors. Since only the relative orientations of the principal axis systems (PAS) at each of the sites matter, the Euler angles can be taken equal to zero for one of the states at each site. This leads to 30 parameters being necessary for describing the hyperfine interactions of the dimer. This number together with two rate constants and one independent occupation number gives a total of 33 parameters.

The hyperfine interactions at the two metal sites are not constant in time but fluctuate as a result of stochastic jumps of the electronic system between states 1, 2, and 3,

$$H_A[Fe^{2+}(1)]\overset{p_d}{\underset{p_u}{\longleftrightarrow}}H_A[Fe^{2+}(2)]\underset{p'}{\longleftrightarrow}H_A[Fe^{3+}(3)] \tag{5a}$$

$$H_B[Fe^{3+}(1)]\overset{p_d}{\underset{p_u}{\longleftrightarrow}}H_B[Fe^{3+}(2)]\underset{p'}{\longleftrightarrow}H_B[Fe^{2+}(3)] \tag{5b}$$

The lack of collinearity between PAS's of the EFG tensors for the two iron sites and the PAS of zero-field splitting tensor for the $S = {}^9/_2$ coupled spin of the ground state suggests the presence of low-symmetry components in the crystal fields at the iron sites and prompted us to use Blume's relaxation theory which includes off-diagonal interactions for simulating the relaxational spectra.[24,25] The relaxation calculations were performed with a program written in MATHEMATICA[26] which evaluates the spectra for the iron sites and adds them in a 1:1 ratio to obtain the spectrum for the dimer.

Apart from the second-order Doppler shift, the electric field gradients and isomer shifts used in the simulations were assigned values independent of temperature. Hence, the temperature dependence of the calculated spectra is determined by the rate constants and the populations of the electronic states. Finding good simulations of multiple spectra (Figure 6) in a 33parameter space is a nontrivial task. Analysis of the high-temperature spectra (293 and 306 K (not shown)) offers the best opportunity to determine the EFG's of the excited states**.** First, the general features of the spectra indicate that they cannot be fit with a two-state model but at least three different electronic states must be involved. Second, the commonly used spin-coupling schemes assume that the excited states of a spin ladder involve approximately the same orbital state as the spin ground state, and therefore, ΔE_Q and δ should not significantly change when excited states of the spin ladder become populated. Since the susceptibility data of **1** indicate the presence of low-lying levels of the spin ladder, we naturally assumed that the EFG-tensors and the isomer shifts of the excited states 2 and 3 were the same as those obtained for the ground state. Adopting the hyperfine parameters for the trapped sites of the ground state, we obtained a simulation of the 293 K spectrum that reproduced qualitative features of the spectra; see Figure 7 (top). It can be seen that the two sites contribute distinct features to this spectrum as illustrated by traces A and B. However, the quantitative agreement between theory and experiment is rather poor. The disagreement can be improved by allowing ΔE_Q-

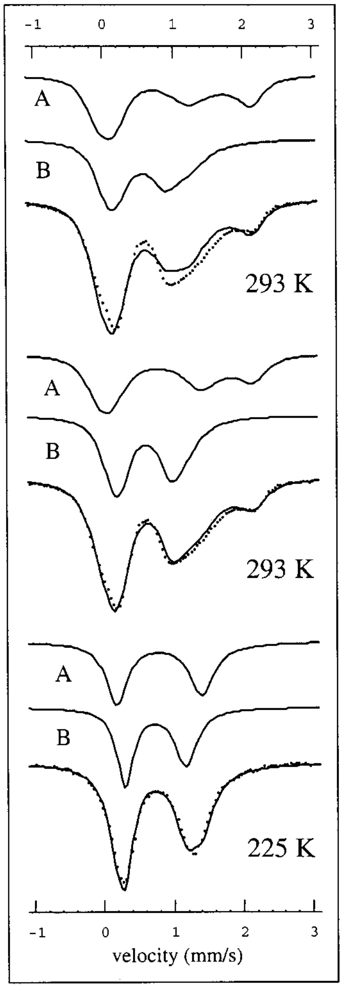

Figure 7. (top) Spectrum for [**1**]·*y*MeCN(powder) (sample 4) at 293 K (dots). Simulation and deconvolution (solid curves) with respect to sites A and B of complex, using ground-state parameter values for Fe^{2+} and Fe^{3+} independent of state and site labels, Euler angle β = 40° between their PAS's, p_u = 1.5 MHz, and p' = 31 MHz; (middle) Spectrum for [**1**]·*y*MeCN(powder) at 293 K (dots). Simulation and deconvolution (solid curves) with respect to sites A and B of complex, using parameters of Tables 6 and 7; (bottom) Spectrum for [**1**]·2DMF(crystal) (sample 2) at 225 K. Simulation and deconvolution (solid curves) with respect to sites A and B of complex, using parameters of Tables 6 and 8.

---

(25) Dattagupta, S.; Blume, M. *Phys. Rev. B* **1974**, *10*, 4540−4550.

(26) Wolfram, S. *Mathematica, a System for Doing Mathematics by Computer*; Addison-Wesley: Redwood City, CA, 1991.

Table 6. Electronic Parameters for Relaxation Analysis of [**1**]·*y*MeCN(powder)

electronic state	iron atom (spin)[e]	δ (mm/s)	ΔE_Q (mm/s)	η[b]	α (deg)[a]	β (deg)[a]	γ (deg)[a]
1	$Fe_A^{2+}(2)$	1.12[c]	−2.34[c]	0.143[c]	0	0	0
1	$Fe_B^{3+}(^5/_2)$	0.55[c,d]	0.90[c]	0.153[c]	0	0	0
2	$Fe_A^{2+}(2)$	1.12	−1.79	0.143	0	50	0
2	$Fe_B^{3+}(^5/_2)$	0.55	0.80	0.153	0	45	0
3	$Fe_A^{3+}(3/2)$	0.65	1.42	0.5	166	56	15
3	$Fe_B^{2+}(2)$	1.12	1.54	0.5	90	25	0

[a] The simulations depend only on the relative angles at each site. The Euler angles are defined in ref.[40] [b] These values are not unique, as a consequence of the ambiguity problem described in ref.[41] For this reason, the Euler angles have not been expressed relative to the PAS of D but to the PAS's of the iron EFG's in state 1. [c] Values obtained from simulation of low-temperature spectra. [d] Replaced by 0.65 mm/s in simulations for [**1**]·2DMF(crystal). [e] Local spins of spin model discussed in Section 4.4.

Table 7. Rates and Line Width Parameters for Relaxation Analysis of [**1**]·*y*MeCN(powder)

temp (K)	p_u (MHz)[a]	p' (MHz)[a]	Γ_A [b](mm/s)	Γ_B [b](mm/s)
100	0.06	1.16	0.37	0.55
125	0.23	1.16	0.32	0.36
150	0.23	1.51	0.32	0.36
174	0.70	1.97	0.30	0.30
195	1.28	4.06	0.24	0.24
225	1.39	5.57	0.23	0.23
250	1.51	9.28	0.22	0.22
265	1.51	11.6	0.22	0.22
293	1.86	18.6	0.22	0.22
306	2.09	20.9	0.22	0.22

[a] 1 mm/s = 11.6 MHz. [b] Line width parameters. (*f w h m*) for Fe_A and Fe_B.

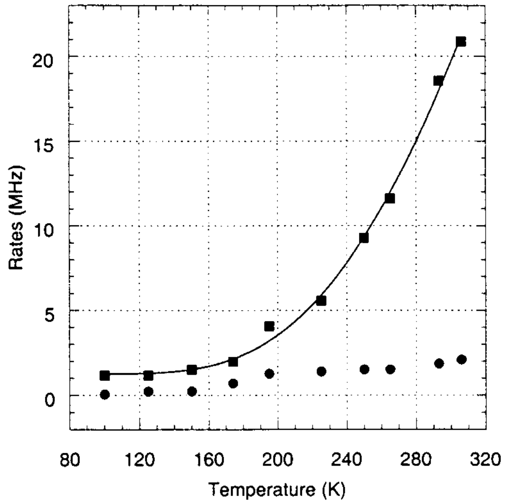

Figure 8. Plot of hopping rate p' (squares) and rate p_u (circles) versus temperature obtained from analysis of relaxational spectra for [**1**]·*y*MeCN(powder) in Figure 6 (squares). Solid curve is a fit of the rates with rate law of eq 7, using $p'_{\text{tunnel}} = 1.25$ MHz, $H_{AB} = 2.2$ cm^{-1}, and $\Delta G^* = 950$ cm^{-1}.

values and to a lesser extent δ-values for the excited states which differ from those obtained for the ground state (see Table 6). The latter parameters give the improved simulations that are shown in the center panel of Figure 7 and in Figure 6. The dependence of the hyperfine parameters on the electronic state implies that states 2 and 3 cannot simply be associated with the excited states of the spin ladder but rather suggests an association with orbital states. (As a note of caution, we remark that the state-dependence of the EFG's listed in Table 6 should be interpreted with the caveat that spurious parameter values may arise from mimicking a complex physical system by a simplified model, like the three-state model.)

The line at 2.3 mm/s Doppler velocity in the [**1**]·*y*MeCN(powder) spectra is a marker for the occupation of state 1 (W_1). On the basis of Lorentzian fits of the spectra in Figure 6 (not shown), W_1 has been estimated at different temperatures. With the caveat that this procedure can only provide a rough estimate of this quantity, the estimates for W_1 are close to the $^9/_2$ state population in **1** inferred from magnetic susceptibility data (e.g., $W_1 \approx 0.4$ at 293 K).[12] This result suggested to us to consider the possibility of identifying state 1 with the $S = {}^9/_2$ ground state of the complex and states 2 and 3 with the lower spin ($S < {}^9/_2$) states of the complex. This assignment implies that the hopping process takes place in the excited spin states. The thermal population of the state 1 can be expressed as

$$W_1 = 10/[10 + 2(8e^{-9x} + 6e^{-16x} + 4e^{-21x} + 2e^{-24x})] \qquad (6)$$

by taking the $^9/_2$ level as the origin of the energy scale and defining x as J'/k_BT. The factor 2 in the excited spin state multiplicities in eq 6 accounts for the two valence states involved in the hopping process. A value for J' of 12.5 cm^{-1} was used to ensure that despite the increase in the weight of the $S < {}^9/_2$ states, these states retain populations equal to those determined by magnetic susceptibility. Equation 6 was used for the simulations in Figures 6, 7 (top), and 7 (middle) and although the relationship may be accidental, the agreement with experiment is very good

Once a good simulation was obtained for the 293 K spectrum, only the rate constants were varied to fit the spectra recorded at lower temperatures. The resulting rate constants are given in Table 7 and plotted in Figure 8 as a function of temperature. The inter-site hopping rate (p') is systematically greater than the rate for transitions between states 1 and 2 ($p_{u,d}$). The hopping rate exhibits a plateau characteristic for tunneling below 150 K and a rapid increase characteristic for a thermally activated process above this temperature (Figure 8). As a consequence, the hopping rate is fast compared to the nuclear precession frequencies of the ^{57}Fe nuclei (fast relaxation) at high temperature whereas the rates between states 1 and 2 remain slow on the Mössbauer time scale throughout the temperature range of measurement. As the ground state (state 1) is kinetically isolated ($p_{u,d}$ slow) from the fast relaxing states 2 and 3 (p' large), these states give rise to distinguishable (localized and averaged) subspectra.

Although inspection of the spectra of [**1**]·2DMF(crystal), shown in Figure 9, suggest merging behavior, a two-state hopping model failed to produce satisfactory simulations of the experimental data. Thus, as a function of increasing temperature, the calculated spectra showed broadening of the middle and rightmost lines, followed by a transformation of these lines into a broad shoulder on the slightly inward moving leftmost line, and eventually a collapse of the shoulder into the rightmost line of an asymmetric averaged quadrupole doublet. The simulations differ from the spectra for [**1**]·*y*MeCN(powder), in that they fail to produce the temperature-independent sigmoidal feature between 0.4 and 1.2 mm/s.

The simulations of the [**1**]·2DMF(crystal) improved dramatically by using the three-state model and the hyperfine parameters for [**1**]·*y*MeCN(powder) (Table 6). The agreement was further improved by increasing the isomer shift $\delta[Fe^{3+}_B(1)]$ by 0.10 mm/s. The resulting simulations for [**1**]·2DMF(crystal) are presented by solid curves in Figure 9. As expected on the basis

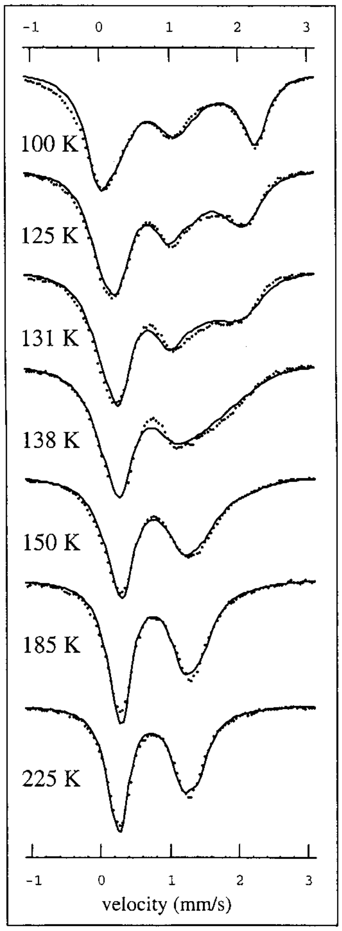

Figure 9. Variable-temperature Mössbauer spectra of polycrystalline sample of [**1**]·2DMF(crystal) (sample 2) (dots) and relaxation simulations (solid curves), based on the three-state model, using electronic parameters and rate constants listed in Tables 6 and 8. Vertical scales of the spectra have been adjusted for presentational purposes.

Table 8. Populations, Rates, and Line width Parameters for Relaxation Analysis of [**1**]·2DMF(crystal) with a Three-state Model.

temp (K)	W_1	p_u (MHz)[a]	p' (MHz)[a,b]	Γ_A [c](mm/s)	Γ_B [c](mm/s)
100	0.75	1.16	1.16	0.35	0.60
125	0.50	5.80	1.16	0.30	0.40
131	0.40	5.80	2.90	0.30	0.30
138	0.25	5.80	6.96	0.30	0.30
150	0.15	3.48	13.9	0.30	0.25
185	0.10	4.64	23.2	0.23	0.23
225	0.05	5.80	31.3	0.23	0.23

[a] 1 mm/s = 11.6 MHz. [b] ΔE_Q- and Δ-values are the same as in Table 6, except for $\Delta(Fe^{3+}{}_B) = 0.65$ mm/s. [c] Line width parameters (*f w h m*) for Fe_A and Fe_B.

of a qualitative comparison of the spectra in Figures 9 and 6, the hopping rates for [**1**]·2DMF(crystal) (Table 8) are greater than the rates for [**1**]·*y*MeCN(powder) at corresponding temperatures. It is noteworthy that the occupation number W_1 did not obey eq 6 but had to be treated as a free parameter to obtain satisfactory simulations of the [**1**]·2DMF(crystal) spectra. As can be seen from Table 8, W_1 decays steeply between 100 and 150 K and almost vanishes at 225 K. The decay behavior suggests that states 2 and 3 acquire a large statistical weight, perhaps as a result of being the representatives for large sets of thermally accessible states with similar electronic properties. At temperatures for which W_1 is practically zero, the three-state model simplifies to a two-state model with hopping taking place between states 2 and 3. The spectra at 185 and 225 K are practically identical, indicating that either the hopping rate p' saturates to a value in the intermediate relaxation regime or sites A and B of the dimer contribute distinguishable quadrupole doublets in the fast hopping limit. The simulations in Figures 6, 9, and 7 (bottom) support the second possibility.

As [**1**]·*y*MeCN(powder) and [**1**]·2DMF(crystal) contain the same structural unit (complex **1**) placed in different environments, it seems plausible that properties which are common to the two aggregates (number of states (≥ 3) and hyperfine parameters) are intrinsic to the complex and properties that change between the two species (occupation numbers and rates) are controlled by the cluster environment. It follows that the three states of the relaxation model correlate with three different states of the complex (electronic or conformational).

Although the performance of the three-state model in the simulations of the relaxational spectra of both [**1**]·*y*MeCN(powder) and [**1**]·2DMF(crystal) is very good, the question may arise as to whether the description given by this model provides a realistic representation of the physical state of these systems or whether it is merely a mathematical fit of the data. An alternative to the three-state model for spectral coexistence may be that the electron hopping takes place in a heterogeneous ensemble of dimers, in which the parameters defining the double-well potentials (Scheme 1) are distributed. To assess experimentally whether such heterogeneity is present, further studies aimed at characterizing the microstructure of [**1**]·*y*MeCN(powder) are presently underway. However, we disfavor this possibility for a variety of reasons. First, our simulations indicate that the three-state model is required for fitting the relaxation spectra for polycrystalline samples of [**1**]·2DMF(crystals), a system with no solvent loss, in which heterogeneity should not be an issue. Second, good simulations for spectra of [**1**]·2DMF(crystal) are obtained by using the values for the electric field gradients extracted from the [**1**]·*y*MeCN(powder) spectra. This coincidence would be rather fortuitous if the spectra of the two species were associated with unrelated distributions in the (temperature dependences of the) hopping rates. Third, it is difficult to reconcile the qualitative features of the relaxation spectra with a static distribution in the asymmetry parameter (see below, Section 4.5).[27]

4.3. Analysis of the Hopping Rates in [1]·*y*MeCN(powder) and [1]·2DMF(crystal). We have analyzed the temperature dependence of the hopping rates between the (quasi) degenerate states 2 and 3, using Marcus' expression for diabatic electron transfer without driving force ($\Delta G^0 = 0$),[28]

$$p' = p'_{\text{tunnel}} + \pi^{1/2}\hbar^{-1}H_{AB}^{av\ 2}(4\Delta G^* k_B T)^{-1/2}\exp[-\Delta G^*/k_B T] \tag{7}$$

The tunneling rate (p'_{tunnel}), the electronic matrix element which couples the donor and acceptor site ($H^{av}{}_{AB}$), and the activation

---

(27) The presence of "dynamic heterogeneity" is compatible with a description based on a homogeneous three-state model. Thus, if the three states of a homogeneous relaxation model correlate with some degree of freedom in the complex-environment subunits, the values for this quantity at a given point of time form a distribution. Viewed from this perspective, the sample can be considered heterogeneous. However, our simulations give poor results if we set the rates p_u and p_d equal to zero (simulations not shown). It follows that the states defining the heterogeneity must have finite lifetimes. Our relaxation model is based on the simplifying assumption that all complex-environment subunits in the sample can be described by a common set of states and rates. In this way, a system with dynamic heterogeneity can be considered homogeneous.

(28) Newton, M. D.; Sutin, N. *Annu. Rev. Phys. Chem.* **1984**, *35*, 437–480.

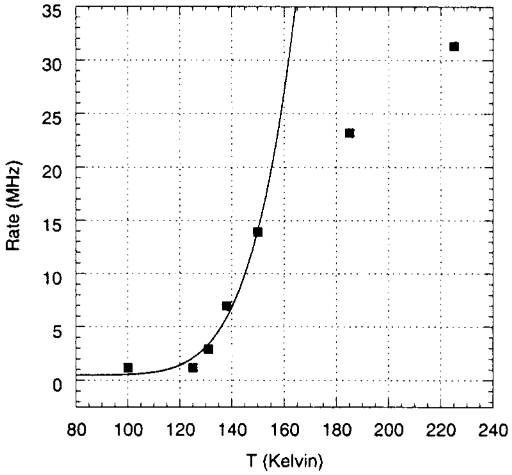

Figure 10. Hopping rate (p') versus temperature obtained from analysis of relaxational spectra for [**1**]·2DMF(crystal) in Figure 10 (squares). Solid curve is fit of rates at temperatures ≤ 150 K with rate law eq 8, using $\Delta G^* = 1110$ cm^{-1} and $\nu_N = 580$ GHz.

energy (ΔG^*) were used as adjustable parameters in the fits. As shown in Figure 8, eq 7 yields an excellent fit of the [**1**]·*y*MeCN(powder) data for $p'_{\text{tunnel}} = 1.25$ MHz (corresponding to a tunneling splitting $\Delta E = 3.6\ 10^{-2}$ cm^{-1}),[29] $H^{av}_{AB} = 2.2$ cm^{-1} and $\Delta G^* = 950$ cm^{-1}.[28] The use of the diabatic eq 7, is consistent with the small value obtained for H^{av}_{AB}.[28]

We have also analyzed the temperature dependence of the hopping rate, using the transition-state-theory expression for adiabatic electron transfer,

$$p' = p'_{\text{tunnel}} + \nu_N \exp[-\Delta G^*/k_B T] \tag{8}$$

where ν_N is a nuclear frequency. The fit of the [**1**]·*y*MeCN(powder) data with eq 8 is of comparable quality as the one obtained using eq 7. Thus, the fits are inconclusive for deciding if the transfer regime is diabatic or adiabatic. The activation energy, $\Delta G^* = 855$ cm^{-1}, obtained for [**1**]·*y*MeCN(powder) is close to the value found using eq 7, and the frequency ν_N is found to be 1.1 GHz.

The hopping rate for [**1**]·2DMF(crystal) cannot be described by an exponential rate throughout the explored temperature range, due to saturation of the rates above ~150 K. However, the rates below this temperature can be approximated by eqs 7 and 8. A fit based on eq 8 of the data set for temperatures up to 150 K yields $\Delta G^* = 1110$ cm^{-1}, $p'_{\text{tunnel}} = 0.5$ MHz, and $\nu_N = 580$ GHz. The simulation is given by the solid curve in Figure 10. Valence averaging in [**1**]·*y*MeCN(powder) and [**1**]·2DMF(crystal) is caused by thermally activated hopping between (quasi) degenerate excited states. This conclusion follows from Figures 8 and 10, according to which $p'_{\text{tunnel}} \ll p'$ in the temperature ranges where the valence averaging occurs. The nuclear frequency in [**1**]·2DMF(crystal) corresponds to an electronic matrix element (H_{AB}) of 50 cm^{-1} in eq 7. Higher values for both ΔG^* and ν_N are obtained when the 150 K point is excluded from the fit. According to eq 8, a large preexponential factor (ν_N) in combination with a large activation energy (ΔG^*) give rise to a steep passage from the localized regime to the delocalized regime along the temperature scale. Indeed, the results for [**1**]·2DMF(crystal) (fast passage; ΔG^* and ν_N large) and [**1**]·*y*MeCN(powder) (slow passage; ΔG^* and ν_N small) are consistent with this relationship. While the change in ΔG^* is moderate (~ 250 cm^{-1}), the values for ν_N differ by more than 2 orders of magnitude. The nuclear frequency for [**1**]·2DMF(crystal) lies in the common vibrational regime, whereas the low value for [**1**]·*y*MeCN(powder) is outside this regime. The origin of the disparity is discussed in Section 4.5.

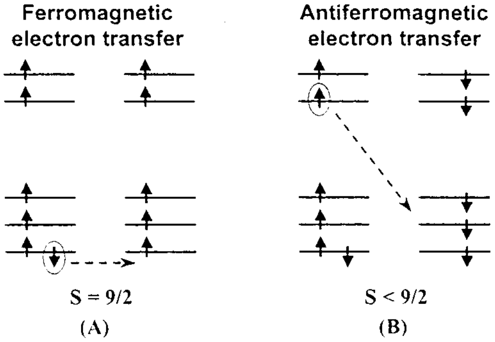

Figure 11. Intramolecular electron-transfer mechanisms in mixed-valence diiron complex with high-spin sites. Spin couplings arising from mechanisms (A) and (B) are called double exchange and antiferromagnetic exchange, respectively. (B) depicts the mechanism for valence averaging described in Section 4.4.

4.4. Spin Control of Electron Hopping.

The analysis in Section 4.2 shows that the relaxation spectra of [**1**]·*y*MeCN(powder) can be simulated by using occupation numbers for the three-state model which are approximately equal to those for subsets of spin states in the temperature range 125 K − 306 K. (In fact, we started our data analyses with the most obvious assumption, namely that the excited states involved were the multiplets of the spin ladder.) However, since the relaxation analysis is independent of the assignment of the states, the coincidence between the occupation numbers may be accidental. In this section we show that assigning relaxation states to spin states has implications that can be used for assessing the validity of this interpretation.

The theory of double exchange predicts that the electronic matrix element for hopping of the “extra” electron (i.e., the electron in the doubly occupied d-orbital) between the metal sites is an increasing function of the total spin quantum number (S) of the complex. Consequently, transfer of the “extra” electron in the excited spin states of **1** is expected to be slower than in the ground state ($S = {}^9/_2$) and thus cannot account for the valence-averaged component observed in Mössbauer spectra in which the $S = {}^9/_2$ ground-state contributes a spectrum characteristic of a localized system. Thus, if excited states of the spin ladder are employed to explain the delocalization phenomenon, a very unusual mechanism must be involved. In contrast to hopping involving a doubly occupied level as depicted in Figure 11A, the matrix elements in the case of hopping of an unpaired electron (Figure 11B), decrease as a function of increasing spin (eq 9).

$$H_{AB}(S) = \beta[(99 - 4S(S+1))/40]^{1/2} \tag{9}$$

The transfer of the unpaired electron is inhibited in the $S = {}^9/_2$ ground state (Figure 11A) but is allowed in the excited spin states, $S < {}^9/_2$ (Figure 11B) as required by the three-state model. As the electronic matrix elements for $S < {}^9/_2$ depend only weakly on spin (eq 9), the error introduced by representing them by the average quantity, H^{av}_{AB}, will remain within acceptable limits. The transfer process can be expressed as

$$[\mathrm{Fe}^{2+}(S_A = 2) - \mathrm{Fe}^{3+}(S_B = {}^5/_2)] \leftrightarrow [\mathrm{Fe}^{3+}(S_A = {}^3/_2) - \mathrm{Fe}^{2+}(S_B = 2)] \tag{10}$$

---

[29] Tunneling splitting is obtained from $\pi^2(\Delta E)^2/h^2\nu$ for a vibration of which $h\nu$ is 300 cm^{-1}.

and involves an alternation of the spin of site A between high spin ($S_A = 2$) and intermediate spin ($S_A = {}^3/_2$) and of the spin of site B between $S_B = {}^5/_2$ and 2. The largest total spin S for which this process is allowed is ${}^7/_2$, i.e., the maximum value attainable by ferromagnetic ordering of the local spins at the right-hand side of eq 10. We designate the process in Figure 11B as "antiferromagnetic electron transfer" by analogy to the related process of "virtual" antiferromagnetic electron transfer, which gives rise to antiferromagnetic exchange contributions ($J \sim H_{AB}^2/U$) to the HDvV Hamiltonian.

Electron transfer can lead to valence averaging only if the level energies of the two groups of states indicated in eq 10 differ by less than k_BT. The free energy change of the process depends on changes in both the intra-atomic Coulomb energies (essentially $E[\mathrm{Fe}^{3+}({}^3/_2)] - E[\mathrm{Fe}^{3+}({}^5/_2)] > 0$) and the crystal-field energies ($-10Dq < 0$) due to intermetal electron hopping between the e_g and t_{2g} levels (Figure 11B). The opposing signs of the intra-atomic and crystal-field energies could lead to the required cancellation

$$E[\mathrm{Fe}_A^{3+}({}^3/_2)\mathrm{Fe}_B^{2+}(2)] - E[\mathrm{Fe}_A^{2+}(2)\mathrm{Fe}_B^{3+}({}^5/_2)] - 10Dq \approx 0 \qquad (11)$$

The condition represented in eq 11 resembles the condition for the spin transition ${}^5/_2 \rightarrow {}^3/_2$ at a ferric ion (second line of eq 12),

$$\begin{aligned} E[\mathrm{Fe}_A^{3+}({}^3/_2)\mathrm{Fe}_B^{2+}(2)] - E[\mathrm{Fe}_A^{2+}(2)\mathrm{Fe}_B^{3+}({}^5/_2)] - 10Dq &\approx \\ E[\mathrm{Fe}^{3+}({}^3/_2)] - E[\mathrm{Fe}^{3+}({}^5/_2)] - 10\mathrm{Dq} &\approx 0 \qquad (12) \end{aligned}$$

where it is assumed that the site energies are additive and dependent on spin but not on site. However, the Mössbauer data for [**1**]·*y*MeCN(powder) and [**1**]·2DMF(crystal) are incompatible with a spin transition. It should be noted that in order to balance the crystal-field splitting in eq 11, the covalent reduction of the energy gap between the spin-quartet and spin-sextet levels at Fe^{3+} must be considerable. The spin quartet in the free ion (^{4}G) lies ~30,000 cm^{-1} above the spin sextet; however energies of about 15 000 cm^{-1} have been reported for Fe^{3+} coordinated to cyclic ligands.[30,31]

The electronic matrix elements describing antiferromagnetic electron transfer ($e_g \rightarrow t_{2g}$) and ferromagnetic electron transfer ($t_{2g} \rightarrow t_{2g}$) involve, respectively, orbitals of different and same symmetry and are therefore expected to be small (ideally zero) and large, respectively. A numerical estimate for the matrix elements can be obtained using the antiferromagnetic exchange parameter for a diferric system[15]

$$J_{AF} = -\frac{2}{25}\sum_i \frac{H_{AB,i}{}^2}{U} \qquad (13)$$

where U is the correlation energy and $H_{AB,i}$ is electronic matrix element for orbital pathway i. For prevailing ferromagnetic exchange, as in compounds **1**, **2**, and **3** (designated in Experimental Section), J_{AF} is smaller than $J_F \sim 10\ cm^{-1}$. By adopting $J_{AF} = -1\ cm^{-1}$ and $U = 10$ eV, a value of ~1000 cm^{-1} is obtained for H_{AB}, which is more than 2 orders of magnitude larger than the empirical value for [**1**]·*y*MeCN(powder), $H^{av}{}_{AB} = 2.2\ cm^{-1}$. For this reason, it is unlikely that the latter value represents the electronic matrix element for the $t_{2g} \rightarrow t_{2g}$ pathway of the ferromagnetic transfer process, and this value seems to support the notion of antiferromagnetic electron transfer (Figure 11B).

The kinetic isolation of state 1 from states 2 and 3, inferred from the application of the relaxational model to the powder samples ($p_{u,d} \ll p'$), is critical for valid identification of these states with spin levels, as it implies a slow inter-spin relaxation rate (at least between the $S = {}^9/_2$ ground state and excited states with $S < {}^9/_2$). Although information about the inter-spin relaxation rates in molecular solids is lacking, it is unlikely that these rates are slow for complex **1**, for the following reasons. First, our EPR studies of **1** show that the relaxation rates between the magnetic substates of each spin multiplet are fast at temperatures where coexistence of spectral components is observed. Second, the zero-field splitting ($D \approx 1.5\ cm^{-1}$)[13] is only one order of magnitude smaller than the exchange parameter ($J' \approx 12\ cm^{-1}$), a circumstance that relaxes the effectiveness of the spin selection rule for inter-multiplet transitions and thus promotes relaxation.

On the basis of the analysis presented in this section, we conclude that identification of the three states of the relaxational model with spin levels is unlikely, despite the small value for the intramolecular electronic matrix element, $H_{AB} = 2.2\ cm^{-1}$, which supports the notion of antiferromagnetic transfer. The main reasons for this conclusion are as follows: (1) The energies of the states in eq 10 must be accidentally degenerate, or nearly so. (2) The transition rates between the spin multiplets must be slow on the time scale of Mössbauer spectroscopy. (3) The isomer shift of the $Fe^{3+}({}^3/_2)$ site in the excited state is unusually high ($\delta \approx 0.65$ mm/s) compared to values quoted in the literature for ferric complexes with an $S = {}^3/_2$ ground state (0.20−0.35 mm/s). (Our attempts to simulate the spectra of Figure 9 with a smaller δ value resulted in less satisfactory solutions.) (4) The different electric field gradients obtained for states 1 and 2 imply an unexpectedly strong dependence of the charge distribution on weak exchange interaction between the metal sites of the complex.

4.5. Conformational Control of Electron Hopping. In this section we will explore a different mechanism, namely, hopping of the "extra" electron (ferromagnetic electron transfer). We assume that interspin multiplet transitions are fast on the Mössbauer time scale. This assumption ensures that the hopping process can be represented by one effective rate parameter denoted p' in the spectral analysis.[32] The electron transfer in **1** is expected to be adiabatic, based on the large value for H_{AB} estimated in Section 4.4. The comparison of the crystal structures of [**1**]·*x*MeCN(crystal) and [**1**]·2DMF(crystal) in Section 4.1 suggested that the marked difference in the hopping rates for the two species is controlled by the asymmetry parameter, E_{as}. The complexes studied here are arranged in a charge-ordered array in [**1**]·*x*MeCN(crystal) ($E_{as} \gg k_BT$), exhibit electron hopping in [**1**]·2DMF(crystal) ($E_{as} = 0$), and show simultaneously features associated with both hopping and trapping in [**1**]·*y*MeCN(powder) and [**1**]·2DMF(crystal). The powder results suggest that upon solvent loss, the asymmetry parameter changes when compared to the one for [**1**]·*x*MeCN(crystal) ($E_{as} \gg k_BT$). We consider three possibilities for [**1**]·*y*MeCN(powder): namely, (i) the asymmetry parameter vanishes in the powders ($E_{as} < k_BT$), (ii) the values for E_{as} have a static distribution, and (iii) E_{as} oscillates randomly as a function of time.

In case (i), the asymmetry parameter would be identical for [**1**]·*y*MeCN(powder) and [**1**]·2DMF(crystal). As the electronic

---

(30) Deaton, J. C.; Gebhard, M. S.; Koch, S. A.; Millar, M.; Solomon, E. I. *J. Am. Chem. Soc.* **1988**, *110*, 6241−6243.

(31) Gebhard, M. S.; Deaton, J. C.; Koch, S. A.; Millar, M.; Solomon, E. I. *J. Am. Chem. Soc.* **1990**, *112*, 2217−2231.

(32) We have adopted here the same symbols to denote the rate constants as in the spin model to highlight the analogy between the two models.

structure of **1** in the two forms is expected to be the same, the differences in the hopping rates can be attributed only to outer-sphere reorganization. However, as discussed in Section 4.1, the increase in ΔG^*_{out} needs to be unrealistically large to produce a difference in hopping rates as that observed between [**1**]·*y*MeCN(powder) and [**1**]·2DMF(crystal). Hence, we consider case (i) to be unlikely.

In case (ii) the powder spectra reflect a static distribution in the asymmetry parameter E_{as}. While loss of solvent and formation of a powder may lead to a distribution in E_{as} which in turn may be the origin of the coexistence observed for [**1**]·*y*MeCN(powder), distributions in E_{as} are expected to be small for [**1**]·2DMF(crystal). Therefore, it would be fortuitous that the coexistence spectra for [**1**]·*y*MeCN(powder) can be simulated by using the three state model and the electronic parameters for [**1**]·2DMF(crystal). Thus, we consider case (ii) to be unlikely as well.

Case (iii) concerns the dynamic properties of the system. During its time evolution, the system executes random motions around the origins of symmetry-breaking coordinates, like q_- in Scheme 1. Passages through the origin of the q_- axis are associated with crossings of the electronic levels. The crossings give rise to electron transfer between the two sites of the complex and, depending on the case, either each individual crossing (adiabatic or strong coupling case) or one out of a multiplicity of crossings (diabatic or weak coupling case) give rise to a transfer event. The asymmetry parameter (E_{as}) can be considered to result from vibronic coupling with a symmetry-breaking coordinate, Q_{as}, which, unlike q_-, is constrained to a narrow interval that excludes the origin. As a result, motions along Q_{as} do not lead to level crossings and associated transfer events on the time scale of the observed transfer process. Thus, in principle, sign flips of Q_{as} (and E_{as}) also give rise to electron transfer but do so at a much lower rate than sign flips of q_-. The slow dynamics of Q_{as} may be due to the presence of high barriers for molecular motion in the potential energy landscape in the vicinity of the complex. However, solvent loss from the crystal liberates motions of the remaining solvate molecules, counterions, and complex ligands that are 'locked-in' in the crystalline form. By "unlocking" E_{as}, the electrons in the powder can hop but do so at a lower rate than in the [**1**]·2DMF(crystal) because the fluctuating asymmetry parameter ($E_{as} > k_BT$) constitutes a rate-limiting control mechanism that is absent in the DMF-containing crystal (for which $E_{as} = 0$). The spectral simulations suggest the involvement of several conformational substates in the hopping process and an entanglement of the electronic and conformational degrees of freedom in the three states of the relaxation model.

The preexponential factors obtained from fitting the rate vs temperature data (Figures 8 and 10) contain important clues about the nature of the electron-transfer mechanism. The factor $\nu_N \sim 10^3$ GHz for [**1**]·2DMF(crystal) is in the vibrational regime. However, the value for [**1**]·*y*MeCN(powder) ($\nu_N \sim 1$ GHz) is about 3 orders of magnitude smaller than for [**1**]·2DMF(crystal). Despite the applicability of the same rate law, the exceptionally low value of ν_N for the powder indicates that the hopping therein is controlled by a mechanism different from that operative in [**1**]·2DMF(crystal). In the discussion of the spin model for coexistence (Section 4.4), the smallness of the preexponential factors for [**1**]·*y*MeCN(powder) samples was ascribed to the off-diagonal character of an $e_g \rightarrow t_{2g}$ transfer process. The present discussion suggests an alternative explanation for the smallness of the preexponential factor, namely an adiabatic process coupled to slow molecular motion (ν_N is small). The strong electronic coupling in this regime allows the electrons to follow the nuclear oscillations so that each nuclear passage through the barrier range results in the transfer of an electron. Nuclear oscillators, such as those in the double wells shown in Scheme 1, change their amplitudes and energies incessantly by random interactions with the medium. According to Kramers' theory,[33] these interactions may turn a fast unidirectional passage, as considered in transition-state theory, into a slow stochastic (or diffusive) walk through the barrier range. Transitions through spatially extended barriers, such as encountered in translational motion of solvent molecules through a crystal, may result in long transition times and thus entail considerable reduction of the transfer rates. This mechanism for reducing the transfer rate may be active in [**1**]·*y*MeCN-(powder) and not in [**1**]·2DMF(crystal) where transition-state theory applies.

Concluding Remarks

In the past fifteen years a significant number of mixed-valence binuclear iron complexes with (N,O) coordination have been synthesized in an effort to generate topological and functional models of active sites in iron-oxo proteins[5,7−12,14,34−36] Analysis of electron delocalization and spin ordering in these complexes indicates a clear correlation between these two electronic properties and their marked dependence on the metal−metal separation. For a few of these complexes, fast electron hopping on the Mössbauer time scale was observed. Interestingly, all but one of the complexes which show thermally activated electron transfer have a valence-localized $S = {}^1/_2$ ground state. Given the recent finding of mixed-valence clusters with $S = {}^9/_2$ ground states in proteins,[17,37−39] we have provided a detailed study of factors which affect the transition to delocalization in the mixed-valence diiron complex with an $S = {}^9/_2$ ground state, $(NEt_4)[Fe_2(salmp)_2]$. The following are the main results and conclusions of this investigation:

(1) $(NEt_4)[Fe_2(salmp)_2]$ crystallizes from acetonitrile/ether with two or three solvate molecules, [**1**]·*x*MeCN ($x = 2,3$). Irrespective of the number of solvate molecules, the complex anion shows crystallographically distinct Fe^{2+} and Fe^{3+} sites at all temperatures between 153 and 293 K. The countercation is in closer proximity to the Fe^{2+} site. This is in contrast to another crystalline form of **1**, [**1**]·2DMF, which at temperatures between 173 and 293 K contains mixed-valence dimers with crystallographically indistinguishable iron sites.

(2) At low temperature, Mössbauer spectra of the crystalline forms considered in this study as well as of powders generated from [**1**]·*x*MeCN, and of solutions of **1** in acetonitrile, are identical and indicate that the valence-localized $S = {}^9/_2$ ground state of the complex is unaffected by the complex anion environment.

---

(33) Kramers, H. A. *Physica* **1940**, *7*, 284−304.
(34) Kanda, W.; Moneta, W.; Bardet, M.; Bernard, E.; Debaecker, N.; Laugier, J.; Bousseksou, A.; Chardon-Noblat, S.; Latour, J.-M. *Angew. Chem., Int. Ed. Engl.* **1995**, *34*, 588−590.
(35) Borovik, A. S.; Que, L. *J. Am. Chem. Soc.* **1988**, *110*, 2345−2347.
(36) Lambert, E.; Chabut, B.; Chardon-Noblat, S.; Deronzier, A.; Chottard, G.; Bousseksou, A.; Tuchagues, J.-P.; Laugier, J.; Bardet, M.; Latour, J.-M. *J. Am. Chem. Soc.* **1997**, *119*, 9424−9437.
(37) Crouse, B. R.; Meyer, J.; Johnson, M. K. *J. Am. Chem. Soc.* **1995**, *117*, 9612−9613.
(38) Hendrich, M. P.; Elgren, T. E.; Que, L. *J. Biochem. Biophys. Res. Commun.* **1991**, *176*, 705−710.
(39) Krebs, C.; Davydov, R.; Baldwin, J.; Hoffman, B. M.; Bollinger, J. M.; Huynh, B. H. *J. Am. Chem. Soc.* **2000**, *122*, 5327−5336.
(40) Arfken, G. *Mathematical Methods for Physicists*; Academic Press: New York, 1970.
(41) Zimmermann, R. *Nucl. Instr. Methods* **1975**, *128*, 537−543.

(3) In contrast to [**1**]·*x*MeCN(crystal), which is valence-localized on the Mössbauer time scale up to 240 K, fast electron hopping occurs for [**1**]·2DMF and [**1**]·*y*MeCN(powder) at temperatures above 100 K. The transition to fast electron hopping takes place over a relatively narrow temperature interval in the case of [**1**]·2DMF. For [**1**]·*y*MeCN(powder) the transition occurs over a wide temperature range and is not complete at 306 K. The relaxational spectra of [**1**]·*y*MeCN(powder) and [**1**]·2DMF(crystal) are superpositions of valence-localized and valence-delocalized components.

(4) The spectral coexistence observed for [**1**]·*y*MeCN(powder) and [**1**]·2DMF(crystal) cannot be explained by a two-state model applied to a homogeneous ensemble of mixed-valence dimers. Use of stochastic line shape theory assuming relaxation processes involving at least three distinct states of the complex anion affords good quality spectral simulations for [**1**]·*y*MeCN-(powder) and for [**1**]·2DMF(crystal) in the transition range.

(5) Analysis of the temperature dependence of the hopping rates for [**1**]·*y*MeCN(powder) and [**1**]·2DMF(crystal) indicate that valence averaging is caused by thermally activated hopping between (quasi) degenerate and distinct excited states. The preexponential factors of the rate laws for [**1**]·*y*MeCN(powder) and [**1**]·2DMF(crystal) indicate that the electron transfer in these systems is controlled by different mechanisms (see Section 4.5).

(6) Quite surprisingly, the ΔE_Q and δ-values of the hopping states 2 and 3 were found to differ from those observed for the ground state. The ΔE_Q and δ-values of states 2 and 3 cannot be explained by assuming that they are associated with excited states of the spin ladder. Moreover, the results obtained for [**1**]·*x*MeCN(crystal) suggest that low-lying orbital states of the ferrous sites are not populated below 250 K. The observation of ΔE_Q- and δ-values for the hopping states that differ from the ground-state parameters suggests some new phenomena that may require modification of the Piepho−Krausz−Schatz model (ref 2). Such an extension is under consideration.

Acknowledgment. This research was supported at Harvard University by NIH Grant 28856 to R.H.H. and at Carnegie Mellon University by NIH Grant 220701 to E.M.

Supporting Information Available: X-ray crystallographic files in CIF format for the compounds in Table 2. This material is available free of charge via the Internet at http://pubs.acs.org.

IC010498L